Data-driven Transient Growth Analysis: With Application to a Transitional Boundary Layer

by

Zhicheng Kai

A thesis submitted in partial fulfillment
of the requirements for the degree of
Master of Science
(Mechanical Engineering)
in the University of Michigan
2024

Thesis Committee:

Aaron Towne, Chair
Jesse Capecelatro

Zhicheng Kai
kaizz@umich.edu
ORCID iD: 0009-0002-3686-2537

DEDICATION

To my girlfriend, Ziyi Zhang, for her love and support, even when she is fighting against aplastic anemia. It is hard to express what level of courage is needed in front of such long-term disease, while all the treatments contain countless side effects and possibilities of relapse deterioration or even death. Now, as she is waiting for the bone marrow transplant, I hope I can give her the faith that everything will get better and better.

I want to express my gratitude to all the medical workers. Without them, the overall survival rate of this disease is less than 40% ten years ago, and now it is over 70%. It is their hard work that shines a light on our human creatures. Besides, this is the first time I realized there are still so many unknowns even about our bodies.

Also, gratitudes are expressed towards those who volunteer to donate their blood. Donating blood might seem minute, but it makes much difference to people who need it.

Finally, a sentence from "Zhuangzi" is cited here:

"吾生也有涯，而知也无涯。以有涯随无涯，殆已！已而为知者，殆而已矣！为善无近名，为恶无近刑，缘督以为经，可以保身，可以全生，可以养亲，可以尽年。"

ACKNOWLEDGEMENTS

I want to extend my deepest gratitude to my advisor, Professor Aaron Towne, whose expertise and insightful feedback were invaluable throughout the research and writing process. His guidance, patience, and unwavering support significantly shaped this work. Thank you for pointing out the right track that made this work possible.

This research would not have been possible without my peer, Peter Frame. Peter, thank you for pointing out my missed mistakes and actively helping with brainstorming. Thanks for your patience in supporting me in understanding the fundamental mathematics and logic to move forward in the project.

I would also like to thank the group members: Rutvij Bhagwat, Ali Farghadan, Junoh Jung, Yuhao Zhou, and James Paulson. Thank you for the active suggestions as I presented my work. Extra gratitude to Yuhao for helping write the code for auto-downloading the data. Without him, the downloading procedure probably might take twice as long.

What's more, gratitude needs to be given to my family, for their support throughout mentally and financially.

In addition, I would like to thank Dr. Amir Danesh-Yazdi, who led me into the path of fluid dynamics through his clear and lively teaching.

Finally, I would like to thank my thesis committee, Jesse Capecelatro, for providing feedback on this thesis.

TABLE OF CONTENTS

LIST OF FIGURES

FIGURE

LIST OF TABLES

TABLE

LIST OF ACRONYMS

CFD computational fluid dynamics

LNS Linear Navier-Stokes Equation

POD Proper Orthogonal Decomposition

DMD Dynamic Mode Decomposition

SVD Singular Value Decomposition

GL Ginzburg-Landau

BL Boundary Layer

DNS Direct Numerical Simulation

JHTDB Johns Hopkins Turbulence Data Base

LSAM Least-Square Approximation Method

CFM Cost Function Method

TLSM Total Least Square Method

IRM Input Regularization Method

DFT Discrete Fourier Transform

ABSTRACT

This thesis develops a data-driven approach to transient growth analysis. The transient growth of perturbations made possible by the non-normality of the linearized Navier-Stokes equations plays an important role in bypass transition. Traditionally, it is quantified via a singular value decomposition of the matrix exponential of the linearized Navier-Stokes operator, requiring direct access to the linearized operator.

In this thesis, we propose a data-driven approach to studying transient growth in which we calculate optimal initial conditions, their responses, and the energy gains between them directly from flow data. We present two equivalent formulations. In the first, inspired by dynamic mode decomposition, data is used to approximate the matrix exponential via a least-squares approximation, and modes and gains are obtained from its singular value decomposition. In the second formulation, the typical definition of energy gain is directly maximized under the assumption that the optimal initial conditions and responses lie within the span of the data. We show rigorously that these two methods are equivalent.

The data-driven method converges to the operator-based solutions with increasing data, provided that the data is noise-free. However, even moderate process or measurement noise levels can lead to large errors. To remedy this, we introduce two regularization methods inspired by the two formulations mentioned above. The first leverages a regularized variant of dynamic mode decomposition, while the second directly regularizes the correlation of the initial conditions to prevent its small eigenvalues, which are generally associated with noise, from creating near-zero denominators in the gain quotient.

We validate the data-driven methods using a Ginzburg-Landau model problem corrupted by process and measurement noise. It is found that the variant of dynamic mode decomposition can produce a consistent result over a range of noise. Meanwhile, regularizing the initial condition can extract decent results over a broad range of the regularization parameters, and outstanding results with some selected regularization values.

Finally, we apply our methods to study the spatial transient growth of distances in a transitional boundary layer using data from the Johns Hopkins Turbulence Database. While previous studies have addressed this problem using locally parallel methods, obtaining and analyzing the non-parallel spatial evolution operator is non-trivial for this problem. The

data-driven method does not suffer from this complication since the simulation data naturally includes the impact of non-parallel evolution. Our method successfully identifies the optimal output response and provides plausible estimates of the transient spatial energy growth at various spanwise wavenumbers.

CHAPTER 1

Introduction

1.1 Motivation

The distinct properties of laminar and turbulent flows significantly impact various engineering disciplines. In aerospace, the transition from laminar to turbulent flow typically results in increased drag, flow separations, heightened noise levels, and more. Conversely, in the energy sector, turbulent flow enhances mixing, thereby improving heat and mass transfer. These phenomena are closely linked to global health and environmental conditions. Consequently, research into predicting the transition from organized laminar flow to highly nonlinear and chaotic turbulent flow is paramount. This topic's importance is underscored by its inclusion in NASA's computational fluid dynamics (CFD) vision 2030 [31].

Pioneering developments in flow stability theories date back to observations made by Reynolds in the 19^{th} century [24]. Early research efforts by Refs. [21, 42, 8] sought to identify natural transition points in flows, whereas others, such as Refs. [41, 18], explored the effects of artificial perturbations. Additionally, the formulation of the Orr-Sommerfeld equation describes the hydrodynamic stability under the parallel flow assumption [19, 32]. The unstable eigenmodes of this Linear Navier-Stokes Equation (LNS) system induce exponential growth in perturbation energy, known as modal growth, as demonstrated by Refs. [36, 28, 30].

However, numerous laboratory experiments have reported significantly lower critical Reynolds numbers than expected [35]. Further research uncovered the phenomenon of algebraic or transient growth, potentially triggering bypass transitions [13, 10, 12]. This growth, stemming from the non-normality of the linear system, can under certain conditions amplify energy to levels that either initiate modal growth or make nonlinear terms relevant, as detailed by Refs. [23, 30, 34]. Transient growth, quantitatively represented by the first Singular Value Decomposition (SVD) mode of the linear time evolution operator, plays a pivotal role in various flow transition scenarios.

Operator-based transient growth analysis has elucidated the physics of flows across dif-

ferent contexts, including parallel shear flow instabilities [22], flow over backward-facing steps [3], and flow through expansion pipes [4]. However, defining the operator is usually nonintuitive: it not only requires a base flow solution but obtaining the operator from the base flow is also hard. The rapid advancement of computational technologies presents a data-driven approach as a viable and promising solution to these challenges. Moreover, data-driven methods often have the advantage of ease of use by obtaining the flow structures directly from data.

1.2 Stability Theories in Flow Transitions

1.2.1 The Navier-Stokes Equation

Flow stability and transition theories have largely been developed based on the LNS equations for infinitesimal perturbation disturbances. In this context, we focus on formulations assuming incompressible and parallel flow conditions. Accordingly, the flow velocity is represented as

$$u_i \to U_i + u_i, \tag{1.1}$$

where U_i symbolizes the parallel base flow solution, and u_i represents the perturbations. Expressing the flow state as a base flow plus perturbations helps to linearize the equation. The linearized momentum equation and the continuity equation for flow perturbations are expressed as

$$\frac{\partial u}{\partial t} + U\frac{\partial u}{\partial x} + vU' = -\frac{\partial p}{\partial x} + \frac{1}{\mathrm{Re}}\nabla^2 u \tag{1.2}$$

$$\frac{\partial v}{\partial t} + U\frac{\partial v}{\partial x} = -\frac{\partial p}{\partial y} + \frac{1}{\mathrm{Re}}\nabla^2 v \tag{1.3}$$

$$\frac{\partial w}{\partial t} + U\frac{\partial w}{\partial x} = -\frac{\partial p}{\partial z} + \frac{1}{\mathrm{Re}}\nabla^2 w \tag{1.4}$$

$$\frac{\partial u}{\partial x} + \frac{\partial v}{\partial y} + \frac{\partial w}{\partial z} = 0, \tag{1.5}$$

where $[x, y, z]$ are the streamwise, wall-normal, and spanwise directions; $[u, v, w]$ are the velocity perturbations in the corresponding directions; p is the pressure perturbation. U is the streamwise velocity from the base flow solution. Since the parallel flow is assumed, the base flow velocities in the other two directions are zero. Equations (1.2) to (1.5) delineate the dynamics of disturbances under the specified assumptions, with the prime symbol ($'$) denoting a derivative with respect to y. Then transform the Navier-Stokes equations into their velocity-vorticity formulation, and apply the Fourier Transform in the homogeneous

directions (x and z), the disturbance evolution is described by Ref. [30]

$$\frac{\partial}{\partial t}\begin{bmatrix}\hat{v}\\ \hat{\eta}\end{bmatrix} = -i\begin{bmatrix}\mathcal{L}_{OS} & 0\\ \mathcal{L}_{C} & \mathcal{L}_{SQ}\end{bmatrix}\begin{bmatrix}\hat{v}\\ \hat{\eta}\end{bmatrix}. \tag{1.6}$$

Here, $\hat{v}$ and $\hat{\eta}$ represent the transformed wall-normal velocity and vorticity, respectively. The operators $\mathcal{L}_{OS}$, $\mathcal{L}_{SQ}$, and $\mathcal{L}_{C}$ correspond to the Orr-Sommerfeld, Squire, and cross-term operators. This equation can be viewed as an initial value problem for small disturbances in viscous flows. Simplifying further, we define $q = [\hat{v}, \hat{\eta}]^T$ and $\mathcal{A} = \begin{bmatrix}\mathcal{L}_{OS} & 0\\ \mathcal{L}_{C} & \mathcal{L}_{SQ}\end{bmatrix}$, leading to

$$\frac{d}{dt}q = \mathcal{A}q, \tag{1.7}$$

and,

$$q_t = e^{\mathcal{A}t}q_0 = \mathcal{M}q_0. \tag{1.8}$$

Here, $q_t \in \mathbb{C}^n$ represents the state q at time t, and q_0 is the initial state. Equations (1.7) and (1.8) lay the foundation for discussing flow stability and energy growth within this paper.

1.2.2 Modal Growth and Transient Growth

The eigenvalues of $\mathcal{A}$ are an indication of the stability of q over time. If all of the eigenvalues have negative real parts, the norm of the state always decays to zero, thus $\lim_{t\to\infty}(\|q_t\|) = 0$. On the other hand, if an eigenvalue has a positive real part, its corresponding eigenmode will grow exponentially. This growth is often referred to as the modal growth. This stability analysis treats the stability as an eigenvalue problem. It is a powerful method that comes directly from the Navier-Stokes operator and mathematically defines the condition of instabilities. However, discrepancies between modal stability analysis and some experimental findings highlight its limitations. For instance, as reported in Ref. [35], the transitional Reynolds number in plane Couette flow can be much lower than the critical Re that causes model growth. Moreover, it has been demonstrated that flows can transition to turbulence even when all eigenmodes are stable. This suggests that flow conditions may become nonlinear before the unstable modes are significantly amplified, named the bypass transition. One possible cause of this is explained by the theory of transient growth.

The linear combination of two non-orthogonal vectors may experience temporal growth, even as the individual vectors decay. A matrix with non-orthogonal eigenvectors is termed non-normal, a common characteristic of $\mathcal{A}$ in fluid systems, particularly in shear flows. Thus, transient growth can be defined as the maximum amplification at time t across all initial

conditions [30], expressed as

$$\begin{aligned} G(t) &= \max_{q_0} \frac{\|q\|^2}{\|q_0\|^2} = \max_{q_0} \frac{\|\exp(\mathbf{A}t)q_0\|^2}{\|q_0\|^2} \\ &= \sigma_1^2\left(\exp \mathbf{A}t\right) \\ &= \sigma_1^2\left(\mathbf{M}\right) \end{aligned} \tag{1.9}$$

where σ_1 represents the first dominant singular value of the matrix exponential $\mathbf{M} := \exp \mathbf{A}t$. This temporal energy growth can be significant enough to render nonlinear terms influential, thereby causing the flow to deviate from linear assumptions. Equation (1.9) is written assuming the two norm. To be more general, $\|q\|^2$ should be written as

$$\|q\|^2 = q^* \mathbf{W} q, \tag{1.10}$$

where $\mathbf{W}$ is the weight matrix. When $\mathbf{W}$ is the identity matrix, $\|q\|^2$ corresponds to the Euclidean norm. This $\mathbf{W}$ can also be understood through defined an observation y. Let $y := \mathbf{L}q$, where $\mathbf{L}^*\mathbf{L} = \mathbf{W}$. Given that the weight matrix is full-ranked, $\mathbf{L}$ always exists. Consequently, the evolution of y is described by

$$\frac{dy}{dt} = \mathbf{L}\mathbf{A}\mathbf{L}^{-1} y. \tag{1.11}$$

The solution to Equation (1.11) is

$$y(t) = e^{\mathbf{L}\mathbf{A}\mathbf{L}^{-1}t} y(0). \tag{1.12}$$

This equation can be further transformed into

$$y(t) = \mathbf{L} e^{\mathbf{A}t} \mathbf{L}^{-1} y(0) = \mathbf{M}_y y(0). \tag{1.13}$$

Therefore, the transient growth, in a more general sense, can be obtained from the singular value square of $\mathbf{M}_y$.

1.3 Data-driven Methods in Fluid Dynamics

With advancements in computational technology, data-driven methods have garnered significant attention in recent years. Proper Orthogonal Decomposition (POD) and Dynamic Mode Decomposition (DMD) are two fundamental techniques for extracting flow structures from data. Refs. [33, 26] offer a clear overview of the principles underlying these methods.

Nevertheless, we provide a brief introduction to them, given their close relevance to our approach.

1.3.1 POD

The POD method decomposes a set of zero-mean data into orthogonal modes. Introduced to the fluid dynamics field by Lumley [17] to identify coherent structures in fluid flows, the aim of POD is expressed as

$$q = \sum_j a_j \phi_j, \tag{1.14}$$

where q represents the state perturbations around zero mean, ϕ_j denotes the POD modes, and a_j are the corresponding coefficients. The physical interpretation of the modes varies depending on the specific definition of q. However, what remains constant is that POD modes are the optimal modes that best represent the data. By employing a limited number of modes and varying coefficients, the flow at different spatial or temporal points can be estimated.

When calculating these modes, a prevalent method is the use of SVD, which for a data matrix $\mathbf{Q} \in \mathbb{C}^{m \times n}$ is expressed as

$$\mathbf{Q} = \mathbf{U}\mathbf{\Sigma}\mathbf{V}^*. \tag{1.15}$$

Here, the symbol $(^*)$ denotes the Hermitian matrix. $\mathbf{U} \in \mathbb{C}^{m \times m}$ represents the left singular vectors, corresponding to the eigenvectors of the matrix $\mathbf{Q}\mathbf{Q}^*$, and embodies the POD modes. Conversely, $\mathbf{V} \in \mathbb{C}^{n \times n}$ relates to the POD modes in the reduced space, represented by the eigenmodes of $\mathbf{Q}^*\mathbf{Q}$. The matrix $\mathbf{\Sigma}$ is a diagonal matrix containing the singular values arranged in descending order, such that $\sigma_1 \geq \sigma_2 \geq \cdots \geq \sigma_m$.

Some variations of this methodology include the Balanced POD proposed by Ref. [25] and spectral POD popularized by Refs. [17, 16, 37]. These extensions broaden the application of the method, enhancing compatibility with flow control strategies and facilitating analysis in the spectral space. This enables the resolution of flow structures within the space-time domain, providing deeper insights into fluid dynamics.

1.3.2 DMD

DMD was first introduced by Schmid [29]. It aims to capture the dynamics of data by closely approximating its evolution matrix. The version of DMD referenced later in this paper is the algorithm presented by Ref. [40], termed "exact DMD."

Similar to Equation (1.14), if we consider representing data that satisfies Equation (1.8)

with a set of DMD modes, $[v_1, v_2, \ldots, v_n]$, the state can be discretely represented as

$$q(t_i) = \sum_j c_j e^{\lambda_j t_i} v_j = \sum_j c_j \mu_j^{t_i} v_j. \tag{1.16}$$

Here, c_j are constant coefficients, and $\lambda_j \in \mathbb{C}$ are interpreted as the eigenvalues of $\mathbf{A}$, determining the growth or decay rate and the oscillation frequency of the DMD modes. Let $y_k,\ k \in [1, m]$ represent the set of observations of the data. If there exists a linear relationship between y_k and y'_k, both belonging to the observation set, such as

$$y'_k = \mathbf{M} y_k. \tag{1.17}$$

then the DMD modes and eigenvalues can be derived directly from the eigendecomposition of matrix $\mathbf{M}$. If the observations with the aforementioned linear relations are specifically selected to be equally spaced in time, it becomes the definition given by Ref. [29].

The challenge then lies in estimating this linear operator $\mathcal{M}$. An optimal estimate, in the least squares sense, can be achieved using the pseudoinverse,

$$\mathbf{M} = y'_k y_k^+, \tag{1.18}$$

where $(^+)$ denotes the pseudoinverse. Since the focus is solely on the eigenmodes of $\mathbf{M}$, the computation of the DMD modes and eigenvalues can be performed in a lower dimension. This approach avoids the need to form the full $\mathbf{M}$ matrix, which is typically computationally intensive. The details are referred to Ref. [40].

1.4 Contribution and Outline

This thesis aims to develop a robust data-driven tool for transient growth analysis that not only captures the transient growth of perturbation energy but also identifies the optimal modes. Additionally, as we apply our method to boundary layer data, we delve into the physics of spatial growth in transitional boundary layers. The major contributions include,

1. Formulated Least-Square Approximation Method (LSAM) based on DMD and Cost Function Method (CFM) based on direction maximizing the gain and showed the equivalency.

2. Proposed TLSM and IRM based on the two formulations, improving the method's noise resistance.

3. Empirically evaluated the method's performance and robustness using the modal problem developed by the GL equation.

4. Applied the method to study spatial transient growth in a transitional boundary layer, demonstrating qualitative agreement with theoretical predictions using data, without the need for linear operators.

The work from Ref. [7] needs to be mentioned here, which is also targeted to obtain a data-driven transient growth analysis through an idea extracted from DMD. However, we think their method deviates from the definition of the optimal transient growth that maximizes energy growth. They only find the optimal perturbation at $t = 0$, then evolve it into the future time. Therefore, we don't think their method has obtained transient growth. Besides, in the spatial case, the linear operator, $\mathcal{A}$, is changing when the final location moves further downstream.

Chapter 2 details our method, introducing two independent inspirations that converge to yield our approach. In Section 2.2, we address the robustness of the method by discussing two distinct regularization strategies derived from our theoretical underpinnings.

In Chapter 3, we validate our method using the GL equation, assessing the impact of parameters m and γ. Moreover, we compare the two regularization methods. These evaluations enhance our understanding of the data-driven approach and its applicability to practical scenarios.

Chapter 4 employs our method to detect spatial transient growth in data from a transitional boundary layer. We first outline the preprocessing steps that prepare the input data, followed by a presentation and comparison of our results with existing literature.

Finally, Chapter 5 explores potential future directions and applications of our method. We discuss possible improvements and additional fields where our approach could be beneficial.

CHAPTER 2

Data-Driven Transient Growth Analysis

2.1 Formulation

Consider the data matrices

$$\mathbf{Q}_0 = [q_{0,1}, q_{0,2}, \ldots, q_{0,m}], \mathbf{Q}_t = [q_{t,1}, q_{t,2}, \ldots, q_{t,m}], \tag{2.1}$$

which make $\mathbf{Q}_0$ and $\mathbf{Q}_t \in \mathbb{C}^{n\times m}$. The columns of $\mathbf{Q}$ are the state vectors, which represent the state at a certain time. Each column is a distinct realization, like the y_k defined in Section 1.3.2. Therefore, we have

$$q_{t,k} = \mathbf{M} q_{0,k}, \tag{2.2}$$

for $k \in [1, m]$. In fluid dynamics, it is common for $n \ll m$. Under this condition, we can assume $\mathbf{Q}_0$ possesses full column rank. Drawing from the dataset, two distinct formulations are introduced: LSAM and CFM. Although these methods stem from different theoretical backgrounds, subsequent analysis demonstrates that they yield identical results. The rationale for presenting both formulations is their implications for distinct regularization strategies.

2.1.1 Least-Square Approximation Method

Similar to DMD, our method relies on two data matrices with linear relationships, as indicated in Equation (1.17). Rewriting Equation (1.17) in terms of our data matrices yields

$$\mathbf{Q}_t = \mathbf{M}\mathbf{Q}_0 \tag{2.3}$$

$$\hat{\mathbf{M}} = \mathbf{Q}_t \mathbf{Q}_0^{+}. \tag{2.4}$$

By appropriately defining the snapshots, the matrix $\mathbf{M}$ becomes the discrete representation of the linear operator $\mathcal{M}$. Hence, in transient growth analysis, the square of its first singular

value represents the optimal transient growth, expressed as

$$G_{LSAM}(t) = \sigma_1^2\left(\hat{\mathbf{M}}\right) = \sigma_1^2\left(\mathbf{Q}_t\mathbf{Q}_0^+\right) \tag{2.5}$$

Assuming $\mathbf{Q}_0$ has full column rank allows for the pseudoinverse to be defined as

$$\mathbf{Q}_0^+ = \left(\mathbf{Q}_0^*\mathbf{Q}_0\right)^{-1}\mathbf{Q}_0^*. \tag{2.6}$$

Additionally, since $\mathbf{Q}_0^*\mathbf{Q}_0$ is Hermitian, we can perform a Cholesky decomposition on it, resulting in

$$\mathbf{Q}_0^*\mathbf{Q}_0 = \mathbf{B}^*\mathbf{B}, \tag{2.7}$$

where $\mathbf{B}$ is invertible. Substituting Equations (2.6) and (2.7) into Equation (2.4) gives

$$G_{LSAM}(t) = \sigma_1^2\left(\mathbf{Q}_t\mathbf{Q}_0^+\right) = \sigma_1^2\left(\mathbf{Q}_t\mathbf{B}^{-1}\left(\mathbf{Q}_0\mathbf{B}^{-1}\right)^*\right). \tag{2.8}$$

By representing the squared singular value as the eigenvalue of the product of a matrix and its Hermitian transpose, and after a series of simplifications, we arrive at

$$\begin{aligned} G_{LSAM}(t) &= \sigma_1^2\left(\mathbf{Q}_t\mathbf{B}^{-1}\left(\mathbf{Q}_0\mathbf{B}^{-1}\right)^*\right) \\ &= \lambda_1\left(\mathbf{Q}_t\mathbf{B}^{-1}\left(\mathbf{Q}_0\mathbf{B}^{-1}\right)^*\left(\mathbf{Q}_0\mathbf{B}^{-1}\right)\mathbf{B}^{*-1}\mathbf{Q}_t^*\right) \\ &= \lambda_1\left(\mathbf{Q}_t\mathbf{B}^{-1}\left(\mathbf{B}^{*-1}\mathbf{Q}_0^*\mathbf{Q}_0\mathbf{B}^{-1}\right)\mathbf{B}^{*-1}\mathbf{Q}_t^*\right) \\ &= \lambda_1\left(\mathbf{Q}_t\mathbf{B}^{-1}\left(\mathbf{B}^{*-1}\mathbf{B}^*\mathbf{B}\mathbf{B}^{-1}\right)\mathbf{B}^{*-1}\mathbf{Q}_t^*\right) \\ &= \lambda_1\left(\mathbf{Q}_t\mathbf{B}^{-1}\mathbf{B}^{*-1}\mathbf{Q}_t^*\right), \end{aligned} \tag{2.9}$$

which further simplifies to

$$G_{LSAM}(t) = \lambda_1\left(\mathbf{Q}_t\mathbf{B}^{-1}\mathbf{B}^{*-1}\mathbf{Q}_t^*\right) = \sigma_1^2\left(\mathbf{Q}_t\mathbf{B}^{-1}\right). \tag{2.10}$$

The left and right singular values of $\hat{\mathbf{M}}$ represent the output and input mode respectively. Or, it can also be understood as the eigenvectors of $\hat{\mathbf{M}}\hat{\mathbf{M}}^*$ and $\hat{\mathbf{M}}^*\hat{\mathbf{M}}$.

To obtain these modes, we can rewrite Equation (2.10) as

$$\hat{\mathbf{M}}\hat{\mathbf{M}}^* = \mathbf{Q}_t\mathbf{B}^{-1}\mathbf{B}^{*-1}\mathbf{Q}_t^* = \mathbf{U}\mathbf{\Lambda}\mathbf{U}^*, \tag{2.11}$$

where $\mathbf{U}$ is the eigenvector of $\mathbf{Q}_t\mathbf{B}^{-1}\mathbf{B}^{*-1}\mathbf{Q}_t^*$, and $\mathbf{\Lambda}$ is the gain described in Equation (2.10). Subsequently, we want to compute the input mode, $\mathbf{V}$. First, we need to write the SVD

representation of $\mathbf{Q}_t\mathbf{B}^{-1}$, which is

$$\mathbf{Q}_t\mathbf{B}^{-1} = \mathbf{U}\mathbf{\Sigma}\mathbf{V}^*. \tag{2.12}$$

Then compute $\hat{\mathbf{M}}^*\hat{\mathbf{M}}$,

$$\hat{\mathbf{M}}^*\hat{\mathbf{M}} = \left(\mathbf{Q}_0\mathbf{B}^{-1}\right)\left(\mathbf{Q}_t\mathbf{B}^{-1}\right)^*\left(\mathbf{Q}_t\mathbf{B}^{-1}\right)\left(\mathbf{Q}_0\mathbf{B}^{-1}\right)^*. \tag{2.13}$$

Substitute Equation (2.12) into Equation (2.13), produces

$$\hat{\mathbf{M}}^*\hat{\mathbf{M}} = \left(\mathbf{Q}_0\mathbf{B}^{-1}\mathbf{V}\right)\mathbf{\Sigma}^2\left(\mathbf{V}^*\mathbf{Q}_0\mathbf{B}^{-1}\right)^*, \tag{2.14}$$

where $\mathbf{Q}_0\mathbf{B}^{-1}\mathbf{V}$ defines the eigenvector of $\hat{\mathbf{M}}^*\hat{\mathbf{M}}$, which defines the input mode. Therefore, the optimal I/O modes are columns in $\mathbf{U}$ and $\mathbf{V}$ corresponding to the first singular value σ_1. In other words, we may define

$$u_{in} = \mathbf{Q}_0\mathbf{B}^{-1}v_1, \tag{2.15}$$

$$u_{out} = u_1 = \frac{1}{\sigma_1}\mathbf{Q}_t\mathbf{B}^{-1}v_1. \tag{2.16}$$

To be more general, we may start from Equation (1.13). By converting y into a data matrix form and applying the pseudoinverse in the LSAM for y, the transient growth is computed as

$$G^W_{LSAM}(t) = \sigma_1^2\left(\mathbf{Y}_t\mathbf{Y}_0^+\right), \tag{2.17}$$

where $\mathbf{Y}_0 = \mathbf{L}\mathbf{Q}_0$ and $\mathbf{Y}_t = \mathbf{L}\mathbf{Q}_t$. Applying the same pseudoinverse technique and converting $\mathbf{Y}$ back to $\mathbf{Q}$, we obtain

$$G^W_{LSAM} = \sigma_1^2\left(\mathbf{Y}_t\mathbf{B}_W^{-1}\mathbf{B}_W^{*-1}\mathbf{Q}_0^*\mathbf{L}^*\right), \tag{2.18}$$

where $\mathbf{B}_W$ denotes the Cholesky decomposition of $\mathbf{Y}_0^*\mathbf{Y}_0 = \mathbf{Q}_0^*\mathbf{L}^*\mathbf{L}\mathbf{Q}_0$. It can also be demonstrated that $\mathbf{B}_W^{*-1}\mathbf{Q}_0^*\mathbf{L}^*$, multiplied by its Hermitian conjugate, results in the identity matrix. Thus, the weighted growth is ultimately expressed as

$$G^W_{LSAM} = \sigma_1^2\left(\mathbf{Y}_t\mathbf{B}_W^{-1}\right) = \sigma_1^2\left(\mathbf{L}\mathbf{Q}_t\mathbf{B}_W^{-1}\right). \tag{2.19}$$

Correspondingly, Equation (2.15) and (2.16) in the weighted case is

$$u_{in} = \mathbf{Q}_0\mathbf{B}_W^{-1}v_{W,1}, \tag{2.20}$$

$$u_{out} = u_1 = \frac{1}{\sigma_1}\mathbf{Q}_t\mathbf{B}_W^{-1}v_{W,1}. \tag{2.21}$$

2.1.2 Cost Function Method

The cost function method, aimed at solving the optimization problem, is based on the definition of transient growth as outlined in Equation (1.9). Consequently, the state vectors q_t and q_0 are represented as

$$q_t = \mathbf{Q}_t \psi \tag{2.22}$$

$$q_0 = \mathbf{Q}_0 \psi. \tag{2.23}$$

By substituting these expressions into Equation (1.9), we derive

$$G(t) = \max_{\psi} \frac{\|\mathbf{Q}_t \psi\|^2}{\|\mathbf{Q}_0 \psi\|^2}. \tag{2.24}$$

Equation (2.24) reinterprets data-driven transient growth as the maximum energy amplification achieved through optimal linear combination coefficients ψ. Given that $\mathbf{Q}_0 \in \mathbb{C}^{n \times m}$ with $n \gg m$, it is likely that $\mathbf{Q}_0$ possesses full column rank. In situations where the denominator might approach zero, regularization techniques are applied, which are detailed in the following section. Assuming the denominator remains non-zero, the optimization problem can be expressed as

$$G(t) = \max_{\psi} \frac{\psi^* \mathbf{Q}_t^* \mathbf{W} \mathbf{Q}_t \psi}{\psi^* \mathbf{Q}_0^* \mathbf{W} \mathbf{Q}_0 \psi}. \tag{2.25}$$

A cost function is formulated as

$$J = \psi^* \mathbf{Q}_t^* \mathbf{W} \mathbf{Q}_t \psi - \lambda \left(\psi^* \mathbf{Q}_0^* \mathbf{W} \mathbf{Q}_0 \psi - 1 \right), \tag{2.26}$$

to solve the maximization problem. Identifying the extremum of the cost function involves solving $\frac{\partial J}{\partial \psi} = 0$. This approach, previously proposed by Ref. [39], translates the problem into two sequential SVDs. Here, we introduce an alternate perspective utilizing the Cholesky decomposition.

Starting from Equation (2.25), we define $\mathbf{B}_W$ as previously outlined in Section 2.1.1. Subsequently, by employing the Cholesky decomposition $\mathbf{W} = \mathbf{L}^* \mathbf{L}$, Equation (2.25) can be expressed as

$$G(t) \approx G_{CFM} = \max_{\tilde{v}} \frac{\tilde{v}^* \mathbf{B}_W^{*-1} \mathbf{Q}_t^* \mathbf{L}^* \mathbf{L} \mathbf{Q}_t \mathbf{B}_W^{-1} \tilde{v}}{\tilde{v}^* \tilde{v}}, \tag{2.27}$$

where $\tilde{v}_W = \mathbf{B}_W \psi$ (and thereby $\psi = \mathbf{B}_W^{-1} \tilde{v}_W$). Following a Rayleigh quotient, the solution is found to be

$$G(t) = \sigma_1^2 \left(\mathbf{L} \mathbf{Q}_t \mathbf{B}_W^{-1} \right). \tag{2.28}$$

Similarly, the I/O modes can be written using the coefficient of the optimal growth, ψ,

$$\begin{aligned} u_{in} &= \mathbf{Q}_0\psi = \mathbf{Q}_0\mathbf{B}_W^{-1}\tilde{v}_W, \\ u_{out} &= \frac{1}{\sigma_1}\mathbf{Q}_t\psi = \frac{1}{\sigma_1}\mathbf{Q}_t\mathbf{B}_W^{-1}\tilde{v}_W. \end{aligned} \tag{2.29}$$

This demonstrates that both methods, as elucidated in Equations (2.19), (2.20),(2.21) and (2.28), (2.29) yield identical results.

2.2 Regularization

As could be anticipated from its connection with DMD, the method derived above is sensitive to noisy data. Building on the two formulations introduced in the previous section, we propose two regularization methods to enhance robustness against noise. TLSM adapts the algorithm from Ref. [6], representing an advancement specifically designed for the DMD method. Conversely, the IRM is elucidated through the framework of the CFM.

2.2.1 Total Least Square Method

Expanding on the algorithmic principles common to DMD techniques, our investigation extends to well-established strategies for managing noise, aimed at enhancing LSAM's robustness against both measurement and process noise. Notably, the TLSM, initially put forward by Ref. [11], marks a significant progression in this area. Ref. [6] later introduced a slightly more efficient and computationally simpler variant, which we have incorporated into our analysis. For completeness, we provide an overview of this TLSM methodology within our discussion.

Our goal is to solve for M in the equation $MQ_0 = Q_t$, using the pseudoinverse to minimize the least squares error. In an overdetermined system, the pseudoinverse is specifically designed to minimize the error in estimating $\mathbf{Q_t}$, which can be articulated as

$$\text{minimizing} \left\|\mathbf{E}_{\mathbf{Q}_t}\right\|_F \text{ in } \mathbf{Q}_t + \mathbf{E}_{\mathbf{Q}_t} = M\mathbf{Q}_0, \tag{2.30}$$

where $\mathbf{E}_{\mathbf{Q}_t}$ represents the residual error in $\mathbf{Q}_t$. The minimization characteristic inherent to overdetermined systems is leveraged by the TLSM approach. In fluid dynamics data, it is common to encounter scenarios where $n \gg m$, contrasting with the $n < m$ condition. To address this disparity, we can simplify the system by truncating POD modes, effectively transitioning from an underdetermined to an overdetermined system. Revisiting Equation (2.30),

for data that exhibit 'suitable and well-behaved' characteristics [6], an inverse dynamic relationship from Q' to Q can be formalized as

$$\mathbf{Q}_0 = \mathbf{M}_{inv}\mathbf{Q}_t, \tag{2.31}$$

where $\mathbf{M}_{inv}$ denotes the inverse dynamics system, estimated by

$$\mathbf{M}_{inv} = \mathbf{Q}_0\mathbf{Q}_t^{+}. \tag{2.32}$$

This 'backward' pseudoinverse approach aims to minimize the error in estimating $\mathbf{Q}_0$ as described by

$$\text{minimizing} \left\|\mathbf{E}_{\mathbf{Q}_0}\right\|_F \text{ in } \mathbf{Q}_t = M(\mathbf{Q}_0 + \mathbf{E}_{\mathbf{Q}_0}). \tag{2.33}$$

In contrast, the TLSM endeavors to minimize both errors concurrently, as explained in Equation (2.34) and further elaborated in Equation (2.35),

$$\text{minimizing} \left\|\mathbf{E}\right\|_F \text{ in } \mathbf{Q}_t + \mathbf{E}_{\mathbf{Q}_t} = M(\mathbf{Q}_0 + \mathbf{E}_{\mathbf{Q}_0}),\ \mathbf{E} = \begin{bmatrix}\mathbf{E}_{\mathbf{Q}_0}\\ \mathbf{E}_{\mathbf{Q}_t}\end{bmatrix}, \tag{2.34}$$

$$[\mathbf{M} - \mathbf{I}] \begin{bmatrix}\mathbf{Q}_0 + \mathbf{E}_{\mathbf{Q}_0}\\ \mathbf{Q}_t + \mathbf{E}_{\mathbf{Q}_t}\end{bmatrix} = 0. \tag{2.35}$$

This approach presupposes the condition of an overdetermined system, $2n < m$. Typically, however, $n > m$, which necessitates reducing the count of the system's POD modes to a size r, thereby ensuring $2r < m$. To solve Equation (2.35), we first perform the SVD of $\begin{bmatrix}\mathbf{Q}_0 + \mathbf{E}_{\mathbf{Q}_0}\\ \mathbf{Q}_t + \mathbf{E}_{\mathbf{Q}_t}\end{bmatrix}$ and then select the leading r POD modes, resulting in

$$\begin{bmatrix}\mathbf{Q}_0 + \mathbf{E}_{\mathbf{Q}_0}\\ \mathbf{Q}_t + \mathbf{E}_{\mathbf{Q}_t}\end{bmatrix} = U\Sigma_{1:r}V^*. \tag{2.36}$$

Equation (2.36) can be represented as a combination of $r \times r$ matrices,

$$\begin{bmatrix}\mathbf{Q}_0 + \mathbf{E}_{\mathbf{Q}_0}\\ \mathbf{Q}_t + \mathbf{E}_{\mathbf{Q}_t}\end{bmatrix} = U\Sigma_{1:r}V^* = \begin{bmatrix}U_{11} & U_{12}\\ U_{21} & U_{22}\end{bmatrix}\begin{bmatrix}\Sigma_1 & 0\\ 0 & 0\end{bmatrix}\begin{bmatrix}V_1^*\\ V_2^*\end{bmatrix} = \begin{bmatrix}U_{11}\Sigma_1 V_1^*\\ U_{21}\Sigma_1 V_1^*\end{bmatrix}, \tag{2.37}$$

With Equations (2.34) and (2.37), the estimation of $\mathbf{M}$ in a reduced space, $\mathbf{M}_r$, is given by

$$\mathbf{M}_r = U_{21}U_{11}^{-1}. \tag{2.38}$$

The algorithm of TLSM is implemented as follows

Algorithm 1: Total least square method

input : $\mathbf{Q}_0$, $\mathbf{Q}_t$
output: G, u_{in}, u_{out}

if $2n > m$ **then**
  $\mathbf{Q}_0 \to \tilde{\mathbf{Q}}_0$, $\mathbf{Q}_t \to \tilde{\mathbf{Q}}_t$; /* Truncate the POD modes to get $\tilde{\mathbf{Q}}_t \in r \times r$ */
$\mathbf{Z} \leftarrow \begin{bmatrix} \tilde{\mathbf{Q}}_0 \\ \tilde{\mathbf{Q}}_t \end{bmatrix}$;
$[\mathbf{U}, \mathbf{\Sigma}, \mathbf{V}] \leftarrow \mathtt{SVD}(\mathbf{Z})$; /* Take the SVD of $\mathbf{Z}$ and get $\mathbf{U} \in [2r, 2r]$ */
$\mathbf{U} \to \begin{bmatrix} \mathbf{U}_{11}\mathbf{U}_{12} \\ \mathbf{U}_{21}\mathbf{U}_{22} \end{bmatrix}$; /* $\mathbf{U}$ can be rewrite into a set of $r \times r$ matrices */
$\mathbf{M}_r \leftarrow \mathbf{U}_{21}\mathbf{U}_{11}^{-1}$;
$[\mathbf{U}_M, \mathbf{\Sigma}_M, \mathbf{V}_M] \leftarrow \mathtt{SVD}(\mathbf{M}_r)$;
$G \leftarrow \sigma_1^2(\mathbf{M}_r)$;
$u_{in} \leftarrow \mathbf{U}_M(1,:)$, $u_{out} \leftarrow \mathbf{V}_M(1,:)$;

2.2.2 Eigenvalue Regularization Method

As discussed in the preceding section, the presence of zero or relatively small eigenvalues (compared to the largest one) in the denominator of $\mathbf{Q}_0^*\mathbf{Q}_0$ can significantly influence the system's output. This issue is further compounded by the presence of noise. One approach to mitigate this concern involves the regularization of the eigenvalues of the positive-definite matrix $\mathbf{Q}_0^*\mathbf{Q}_0$, which is expressed as

$$\left(\mathbf{Q_0^*Q_0} + \gamma\mathbf{I}\right)\psi = \psi \begin{bmatrix} \sigma_1^2 + \gamma & & \\ & \ddots & \\ & & \sigma_n^2 + \gamma \end{bmatrix}, \tag{2.39}$$

where $\gamma \in \mathbb{R}$ serves as the regularization factor, setting a minimum threshold for the eigenvalues. This adjustment reduces the impact of smaller eigenvalues in the denominator, effectively addressing the distortions introduced by noise. Given that smaller eigenvalues are often primarily associated with noise, this regularization method efficiently suppresses such unwanted elements without negatively affecting the data critical to flow information. We suggest that γ should be selected to fall between the largest and smallest eigenvalues of $\mathbf{Q}_0^*\mathbf{Q}_0$, to ensure minimal interference with essential data. The strategy for choosing γ will be further detailed in subsequent sections, demonstrating that the range of suitable γ values

is quite broad. The algorithm then involves performing the Cholesky decomposition on the regularized matrix $(\mathbf{Q}_0^*\mathbf{Q}_0 + \gamma\mathbf{I})$, expressed as

$$\mathbf{B}^*\mathbf{B} = (\mathbf{Q}_0^*\mathbf{Q}_0 + \gamma\mathbf{I})\,. \tag{2.40}$$

The IRM is implemented as follows:

Algorithm 2: IRM

input : $\mathbf{Q}_0$, $\mathbf{Q}_t$, γ
output: G, u_{in}, u_{out}

$\mathbf{B} \leftarrow \texttt{Chol}\,(\mathbf{Q}_0^*\mathbf{Q}_0 + \gamma I)$; `/* Take the Cholesky decomposition */`
$[\mathbf{U}, \mathbf{\Sigma}, \mathbf{V}] \leftarrow \mathbf{Q}_t\mathbf{B}^{-1}$;
$\psi \leftarrow \mathbf{B}^{-1}\mathbf{V}$; `/*` ψ `is the coefficients to obtain optimal response */`
$G \leftarrow \sigma_1^2$; `/*` σ_1 `is the largest singular value in` $\mathbf{\Sigma}$ `*/`
$u_{in} \leftarrow \mathbf{Q}_0\psi$, $u_{out} \leftarrow \mathbf{Q}_t\psi$

CHAPTER 3

Validation With GL Equation

In this chapter, we apply our method to data generated by the GL equation to assess the correctness and robustness of our approach. The GL equation is a simple linear modal containing a temporal energy growth with its operator defined analytically. Therefore, it is a good tool for us to validate our data-driven estimations by comparing them with the operator-based results. In Section 3.1, the GL equation and the corresponding parameters are introduced, which generate our dataset. Error metrics are included in Section 3.3, where we proposed methods to evaluate our results according to the operator-based results. In Section 3.2, we discuss the preprocessing steps required to format the data for our algorithm. In Section 3.4, we first establish the criteria used to evaluate our methods. Then, we demonstrate how the unregularized method, the TLSM, and the IRM perform under various parameter choices.

3.1 Ginzburg-Landau Equation

The GL equation is formulated as

$$\begin{aligned} &\frac{\partial q}{\partial t} = \mathcal{A}q = \left(-\nu\frac{\partial}{\partial x} + \gamma_g\frac{\partial^2}{\partial x^2} + \mu\right) q, \\ &q(x,t) < \infty \quad \text{as } x \to \pm\infty, \end{aligned} \tag{3.1}$$

where ν and γ_g are the flow convection and dissipation coefficients, respectively, and $\mu = \mu_0 - c_u^2$ represents the characteristic of exponential instability in the equation. The matrix $\mathcal{A}$ combines the evolution factors into a single operator. The state generation code is based on the model described by Ref. [2]. In this study, we used $\mu_0 = [0.2, 0.38, 0.4]$. A value of $\mu_0 = 0.2$ models a modest transient growth of the initial state. With $\mu_0 = 0.38$, the state experiences significant growth but ultimately decays. However, at $\mu_0 = 0.4$, the state is unstable and continues to grow over time. For our applications, we selected $\mu_0 = 0.38$ and

other parameters that are consistent with Ref. [2]. Figure 3.1 provides a sample visualization of the state with these μ values.

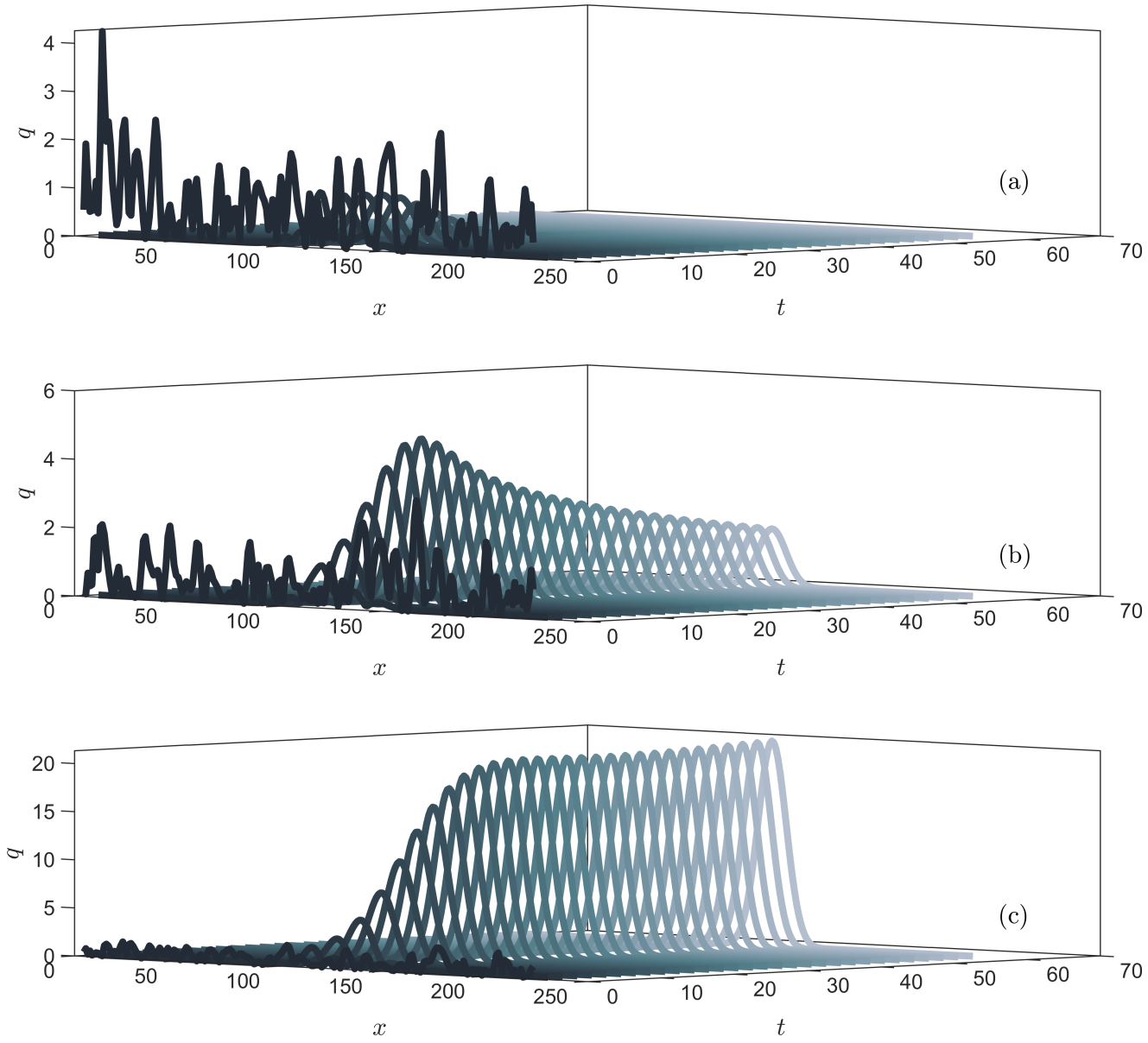

Figure 3.1: The output from GL equation with $\mu_0 = [0.2, 0.38, 0.4]$.

For further discussions, multiple runs with various random initial conditions were conducted. These initial conditions have zero mean, a variance of $var(q_0) = 1$, and a spatial correlation length, λ, of 2. The initial condition is further discussed in Section 3.2.1. This randomly generated state vector is also utilized for simulating measurement and process

noise.

3.2 Data Matrix Construction

Given the definition of the data matrix as presented in Equation (2.1) and further elaborated in Section 1.3.2 and by Ref. [40], two key elements are required to extract the transient growth, $G(t)$, over time. Firstly, the data pair $q_{0,i}, q_{t,i} \in \mathbb{C}^n$ $n = 220$, must span the time range of interest. Secondly, a sufficient number of realizations, m, is necessary so that our system can span the space that maximizes growth. Moreover, there are no restrictions on the relationships between $q_{0,i}$ and $q_{0,j}$, for $[i, j] \in [1, m]$. There are two options to construct the state matrices. One is to perform a single iteration over time, and then the state defined in Equation (2.1) becomes

$$\mathbf{Q}_0 = [q_0, q_1, \ldots, q_{m\Delta t}]\,; \mathbf{Q}_t = \left[q_t, q_{(1+t)}, \ldots, q_{m\Delta t+t}\right]. \tag{3.2}$$

The state matrices are chosen from neighboring times. However, we have an overall decaying system, with a temporal growth initially. This indicates the domination of slow decaying modes in a long time block. Meanwhile, the number of realizations is essential for spanning the energy space, further enforcing the length of the time block. This method might likely overlook the transient modes. Instead, our approach involves conducting m time evolutions, each with a duration $T = Nt \times dt$, and each starting from different initial conditions, where $q_{t,i}$ are all from different time-iterations but at the same time location, t. This enables us to span the space better and capture the transient physics.

3.2.1 Initial Conditions

To ensure our initial conditions are both physically plausible and varied across different realizations, we employed an algorithm provided by Ref. [9], which generates random initial conditions with Gaussian spatial correlations. The spatial correlation is defined by a Gaussian function, as expressed in

$$C_{i,j} = \mathbb{E}\left[q(x_i), q(x_j)\right] = e^{\left(\frac{x_i - x_j}{\lambda}\right)^2}, \tag{3.3}$$

where $q\left(x_i\right)$ denotes the state at the spatial coordinate x_i, and λ represents the correlation length. Figure 3.2 presents several representative examples of the initial conditions utilized in our study. We selected $\lambda = 2$ for our parameters.

Each initial condition depicted in Figure 3.2 forms one column of $\mathbf{Q}_0$. Using these initial

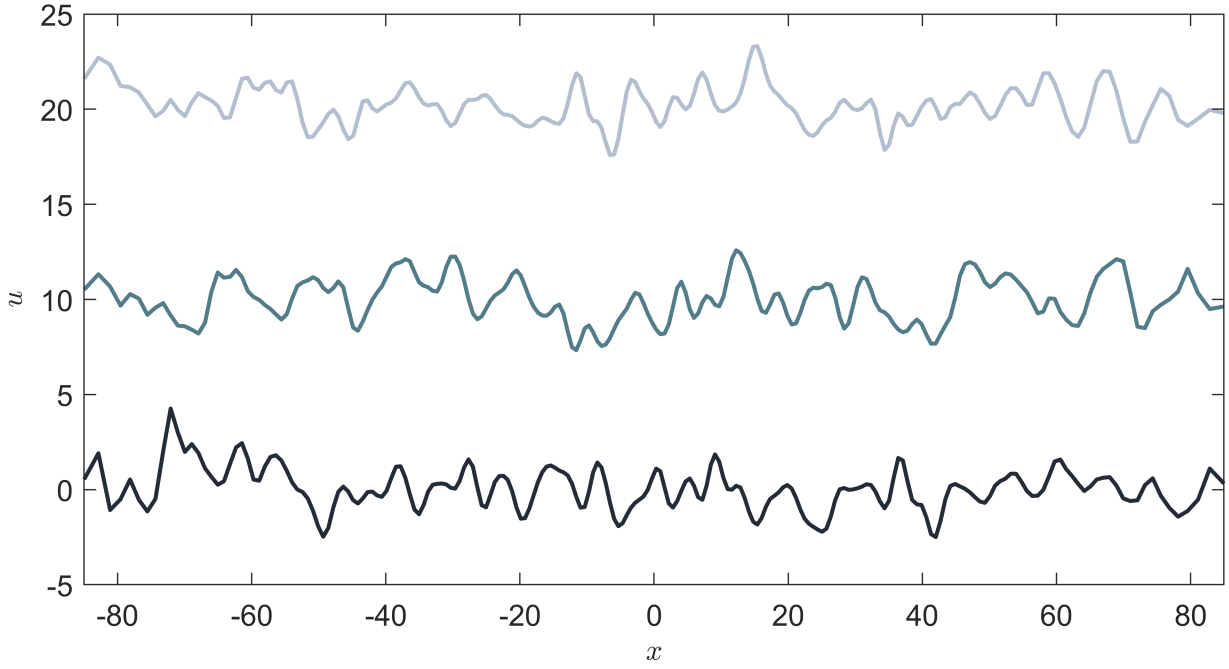

Figure 3.2: Initial condition with parameters $\lambda = 2$. Three examples are shown here. For Illustration purposes, the magnitude of each has been increased by 10 (all curves are zero mean).

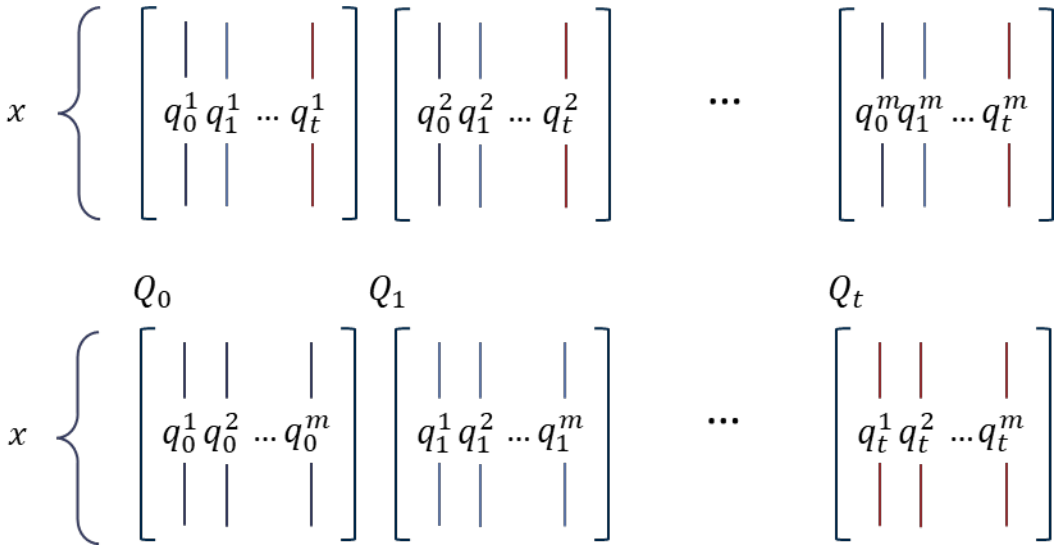

Figure 3.3: The process of constructing the input matrix. The matrices in the first row represent different simulations, with each column color-coded according to its position in time. These columns are reorganized by time in the second row, forming $\mathbf{Q}_0$ and $\mathbf{Q}_t \in \mathbb{R}^{n \times m}$.

conditions, we evolve each one over time to generate $\mathbf{Q}_t$. As illustrated in Figure 3.3, the first row shows that each matrix represents one time evolution, with a total of m such evolutions. In the second row, we rearrange each column from the first row according to their temporal sequence. This reorganization creates our input matrix.

3.2.2 Measurement and Process Noise

The robustness of the methods is a crucial factor in determining their applicability. To assess the resistance of our regularization methods to noise, we introduced both measurement and process noise into the data. These two types of noise are incorporated into the system as follows

$$\frac{dq}{dt} - \mathbf{A}q = W, \tag{3.4}$$

$$q' = q + N, \tag{3.5}$$

where W represents process noise, and N denotes measurement noise. Here, q' signifies the state including the measurement noise. The noises were generated based on the same method discussed to create the initial condition. In addition, the process noise is band-limited in time with cuton and cutoff frequencies of $[0.001, 0.5]$.

The specific values of the parameters selected in Section 3.2 are not critical. The values we used were chosen to ensure consistency and formality in our evaluation setup.

3.3 Error Metrics

Given our knowledge of the GL operator, it is possible to calculate an analytical optimal growth along with the corresponding mode. Based on this, we proposed several metrics for comparing our data-driven output with the analytical results.

Peak percent difference (ϵ_p): This metric quantifies the relative discrepancy between the peak transient growth values predicted theoretically ($G_{\max,AN}$) and those obtained via the data-driven models ($G_{\max,DD}$). It is defined as

$$\epsilon_p = \frac{G_{\max,DD} - G_{\max,AN}}{G_{\max,AN}}, \tag{3.6}$$

where the subscript DD refers to data-driven results, and AN refers to analytical outcomes. This measure offers insight into the precision of peak growth predictions by the data-driven methodologies.

Input/output mode error (ϵ_i): A standard method for comparing two vectors involves calculating

$$\epsilon_i = 1 - \frac{|\langle u_{DD}, u_{AN}\rangle|}{\|u_{DD}\| \, \|u_{AN}\|}, \tag{3.7}$$

where u can represent either u_{in} or the output mode u_{out}. This metric is utilized to assess the accuracy of input/output mode estimations.

3.4 Results

3.4.1 Effect of the realization number

The number of realizations, m, represents the count of independent state vectors evolving over time or space, serving essentially as the sample size in the direction of evolution. Ideally, a larger number of samples leads to more accurate results. However, an increase in m not only escalates computational costs but may also amplify noise if present. Since transient growth is characterized by the square of the largest singular value of the linear operator matrix, capturing the full dimension of the state is not required. It is widely recognized that working within a reduced space is adequate for accurately determining transient growth. In the context of data-driven methods, the choice of m may be constrained by the dataset at hand, highlighting the need for a technique that is effective across various m values.

To start with, it is useful to evaluate the impact of m in the absence of noise. Figure 3.4 illustrates the transient growth and its optimal modes for $m \in [55, 220]$ using the unregularized method. The transient growth plot indicates that the estimation improves as m

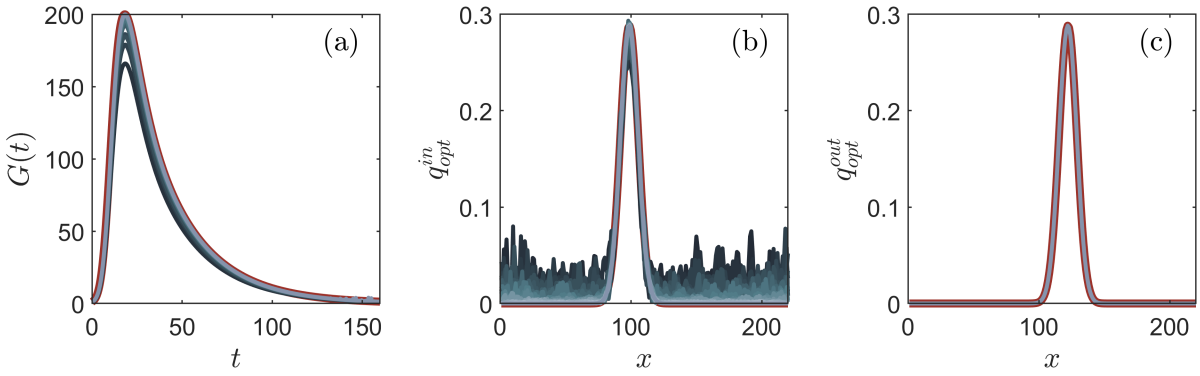

Figure 3.4: Transient growth and the optimal I/O modes with clear data. (—) represent $m = 55$, which transitions into (—) as m increases to 220.(—) is the analytical results obtained from the operator.

increases, with smaller m values yielding lower growth rates. The input mode results are less accurate due to the input mode existing in the full space, whereas the operations are conducted in a reduced space. An exact match with the input mode is achieved when $n = m$. Conversely, the results for the output mode closely align with the analytical outcome for all values of m.

However, what occurs when noise is present? Subsequently, moderate noise levels ($|\mathbf{W}| = |\mathbf{N}| = 0.03$) are introduced. The IRM with $\gamma_{\max} = \frac{n}{m}\gamma = [0, 50, 100]$ and the TLSM are chosen for comparison. We introduce a γ_{max} here to establish a linear relationship between m and γ. This approach is taken because the eigenvalues increase roughly linear according to m. Moreover, typically we aim to avoid making m larger or close to n as additional realizations would become redundant and computationally inefficient. However, for the sake of exploration, we experimented with $m = [55, 110, 165, 220]$, which are ranging from $\frac{1}{4}n$ to n. As shown in Figure 3.5, larger m increases the potential of the growth regardless of the regularization method used. With IRM, a larger γ can better mitigate the noise, but the growth can be underestimated. It can provide a reasonable estimation of $G(t)$ across a range of m values within a certain γ range. Comparing the dotted lines in Figure 3.5 (a), (b), and (c), we can observe that the estimated growth is very noisy for the unregularized method. While in (b), with a slightly higher γ, the curve gets the peak well but still shows some noise at high t. Using an even larger γ, as shown in (c), the noise at high t becomes lower in amplitude, however, it undershoots the peak growth. The TLSM, on the other hand, is more reliant on the choice of m. It shows a high level of noise with a large m. At the m that it can estimate the peak correctly, there are still large noises at high t. When m

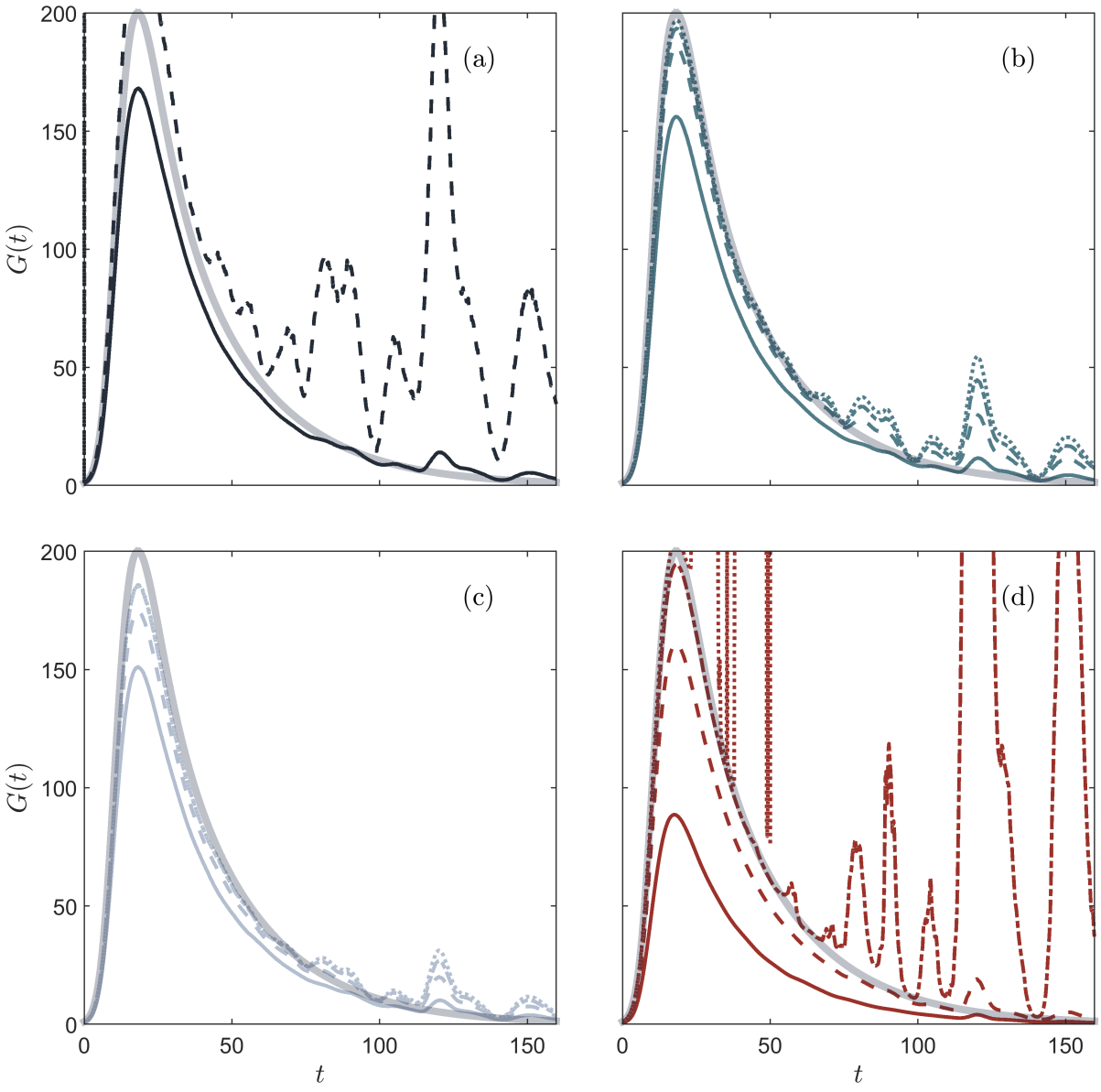

Figure 3.5: Example results of transient growth over time. The line style —, - - -,-·-·and ····, separately represents $m = [55, 110, 165, 220]$. The color ■, ■, ■and ■, individually shows the $\gamma_{max} = [0, 50, 100]$ and the TLSM.

gets low enough that the noisy data at high t disappears for TLSM, it also undershoots the peak. Still, we can conclude that with an appropriate selection of m, the TLSM can also yield reasonable estimations of $G(t)$. Figure 3.6 graphically presents the error metrics ϵ_p and ϵ_i. The analysis of ϵ_p indicates that the TLSM yields better results at lower m values but experiences a significant decline in performance as m surpasses a certain threshold,

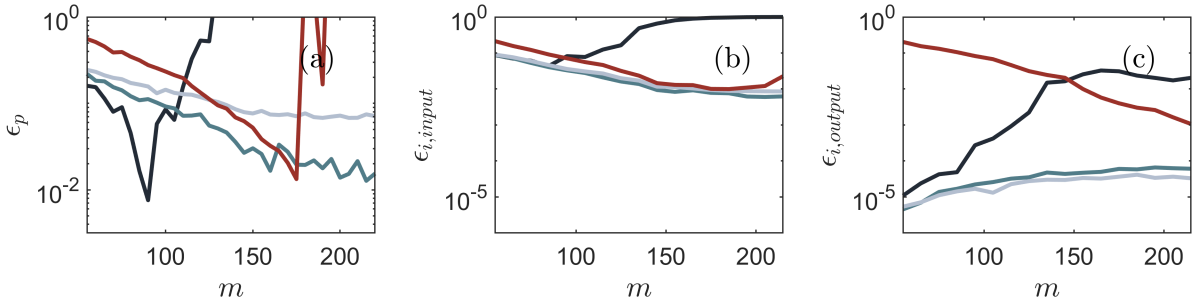

Figure 3.6: (a) ϵ_p of the growth, and ϵ_i of the (b) input and (c) output modes. The color scheme is the same as in Figure 3.5.

particularly for $m > 180$ in this case. On the contrary, the IRM with $\gamma_{max} > 0$ showcases remarkable stability with increasing m, surpassing the TLSM in most scenarios.

The trend for ϵ_i is similar for the IRM but not for the TLSM. As depicted in Figure 3.6, the IRM demonstrates an improvement in accuracy with higher m and γ. However, the TLSM exhibits superior performance at larger m values. This suggests that an increased number of realizations positively impacts mode capture. Furthermore, since an additional estimation is required for the input mode, accurately predicting this mode proves significantly more challenging.

Furthermore, when comparing the IRM with varying γ values to the TLSM, we can conclude that the TLSM offers consistent results. However, the IRM can achieve better estimations with a careful selection of γ. This observation underscores the importance of conducting a more detailed investigation into the optimal choice of γ, which will be discussed in the following section.

3.4.2 Effect of the Regularization Parameter

As previously mentioned, we select our γ by assuming a linear relationship between γ and m, such that $\gamma = \frac{m}{n}\gamma_{max}$. We determine γ_{max} based on the eigenvalues of $\mathbf{Q}_0^*\mathbf{Q}_0$. The sensitivity of the method stems from the significant disparity between the maximum and minimum eigenvalues of $\mathbf{Q}_0^*\mathbf{Q}_0$. The smallest eigenvalues can be easily affected by noise, but after applying the pseudoinverse, their influence significantly increases. The IRM introduces a regularization factor to mitigate the disparity in magnitude between the largest and smallest eigenvalue. Consequently, the range of γ_{max} is defined to lie between the maximum and

minimum eigenvalues, which can be expressed as

$$\gamma_{max} \in [\lambda_n \left(\mathbf{Q}_0^* \mathbf{Q}_0\right), \lambda_1 \left(\mathbf{Q}_0^* \mathbf{Q}_0\right)]. \tag{3.8}$$

In exploring the impact of the regularization parameter γ, Figure 3.7 demonstrates how the peak percentage error fluctuates with different γ_{max} values and m, depicted on a logarithmic scale. The range of γ_{max} showed is in the range of $[0, 100]$, while $\lambda_1 \left(\mathbf{Q}_0^* \mathbf{Q}_0\right) \approx 3000$. It is observed that for m values exceeding a particular threshold, approximately $m \approx 70$, a wide range of γ values effectively regularizes the data, reducing the error to below 10%.

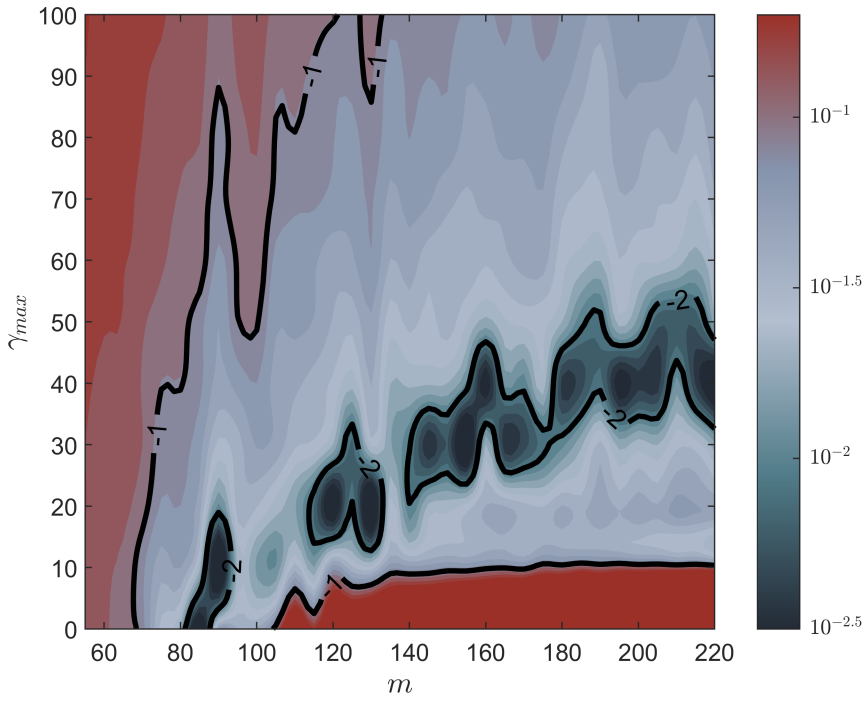

Figure 3.7: ϵ_p for varying γ_{max} and m under the same noise condition as in Figure 3.5. $\epsilon_p = 10^{-2}$ and $\epsilon_p = 10^{-1}$ marked out.

However, ϵ_i exhibits varied dependencies on γ and m. As shown in Figure 3.8, the error for both I/O modes is predominantly determined by the number of realizations. A higher m leads to a lower error for the input mode, while a smaller m favors the output mode. This suggests that estimating the input mode entails estimating the higher dimensional data with lower dimensions, inherently resulting in a higher baseline error. The advantages of increased flow information from a larger m surpass the incremental error. In contrast, the output mode can be estimated accurately with fewer realizations, and larger m values negatively affect

the results by introducing noise. These observations regarding ϵ_i also indicate that there is a flexible range for selecting γ, as long as it is above a specific threshold.

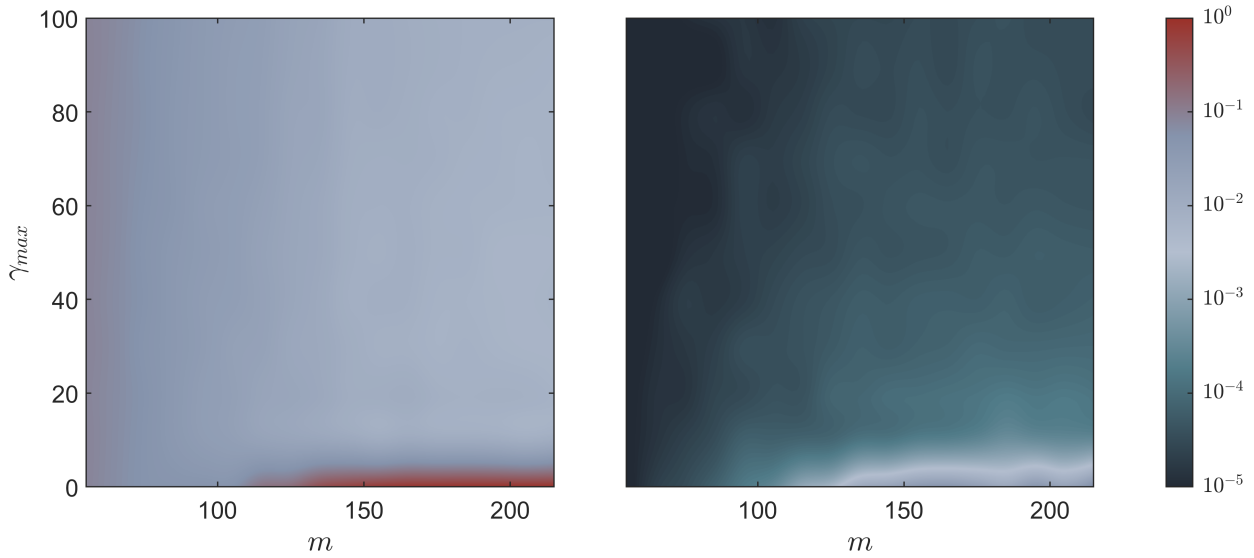

Figure 3.8: Variation of ϵ_i with different γ_{max} and m for (a) input mode and (b) output mode.

Subsequent analysis involved selecting typical γ values to evaluate their effectiveness across different levels of process and measurement noise, with the TLSM serving as a benchmark for comparison. The results, depicted in Figure 3.9 (a), show that an unregularized approach ($\gamma = 0$) may align perfectly with analytical predictions in the absence of noise. However, its effectiveness decreases as noise levels increase. Figures 3.9 (b) and 3.9 (c) examine scenarios with $\gamma_{max} = 50$ and $\gamma_{max} = 100$, respectively. Both configurations demonstrate the ability to accurately estimate maximum transient growth in the presence of noise, whereas the TLSM also provides consistent outcomes, albeit with slightly higher errors.

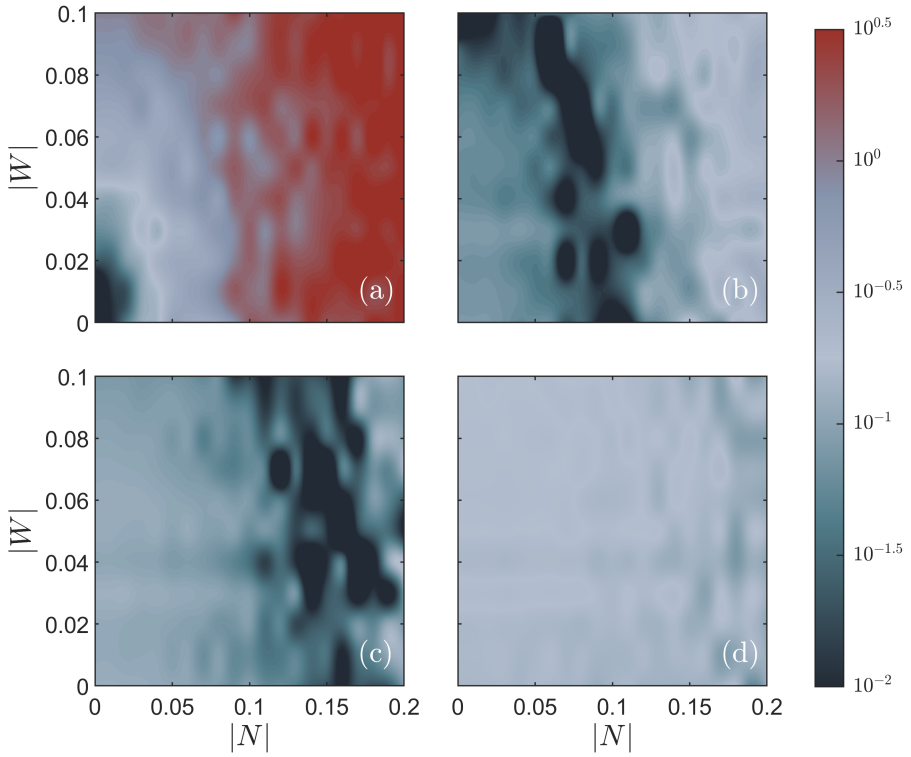

Figure 3.9: ϵ_p of TLSM and IRM with $m = 110$, and (a) $\gamma_{max} = 0$,(b) $\gamma_{max} = 50$,(c) $\gamma_{max} = 100$.

Figure 3.10 presents similar findings for both IRM and TLSM. This analysis confirms that, for the GL equation, our method delivers reasonable results within a flexible parameter range. The next section will apply this methodology to transitional boundary layer data, further demonstrating its applicability and robustness.

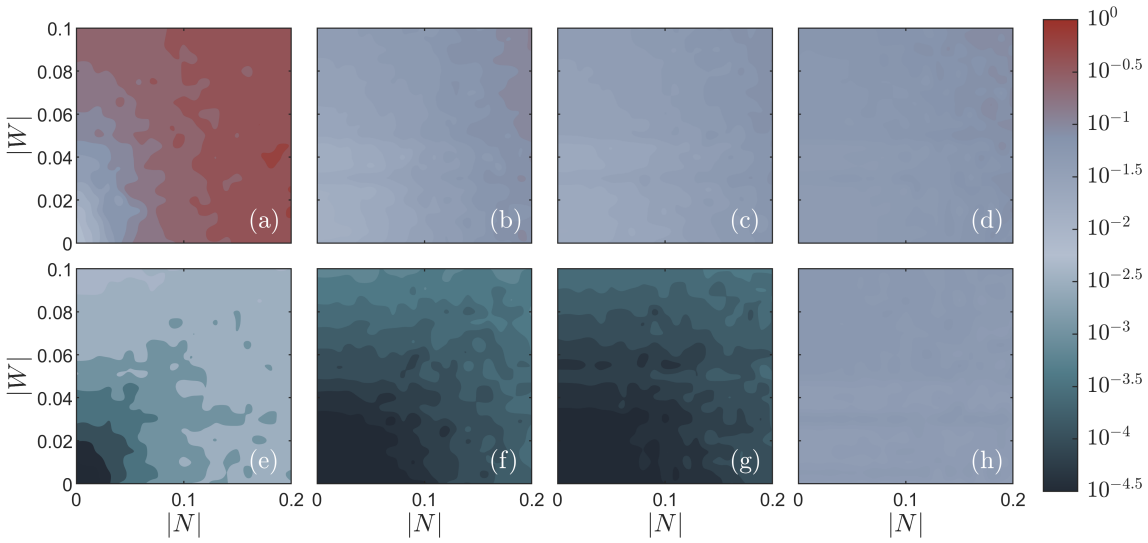

Figure 3.10: ϵ_i of TLSM and IRM for input mode on the first row and output mode on the second. From left to right $\gamma_{max} = [0, 50, 100]$, and the last column is the TLSM. All cases were run with $m = 110$.

CHAPTER 4

Spatial Transient Growth in Transitional Boundary Layer

Previous sections have demonstrated the robustness of our method with the GL equation. In this chapter, we aim to address a less-explored area: spatial transient growth in a non-parallel boundary layer.

According to Refs. [1, 30], the state vector in the spatial case can be assumed to be

$$q(x, y, z, t) = \hat{q}(x, y) \exp[i(\beta z - \omega t)], \tag{4.1}$$

where q is the state vector, $\hat{q}$ is the state after transformed into the frequency domain. This enables Equation (1.7) to be solved by constructing the eigenmodes to $\mathcal{A}$. In the later discussions, the ($\hat{}$) is dropped for simplicity. Ref. [1] provide another assumption: with a relatively high-level free-stream disturbance, which is elongated in the streamwise direction and varies slowly with time, the equations can be considered steady. Therefore, an input-output view of the state is considered as

$$q_x = \mathbf{M}_x(x) q_0. \tag{4.2}$$

The operator is now dependent on x, which makes the method from Ref. [7] not applicable. Meanwhile, the procedure of defining this operator $\mathbf{M}_x(x)$ is hard, but our method can be used on the simulated data directly.

In this chapter, we first describe the dataset, then outline the details of the preprocessing steps in Section 4.2, followed by the presentation of nondimensionalization and the results in Section 4.3 and 4.4.

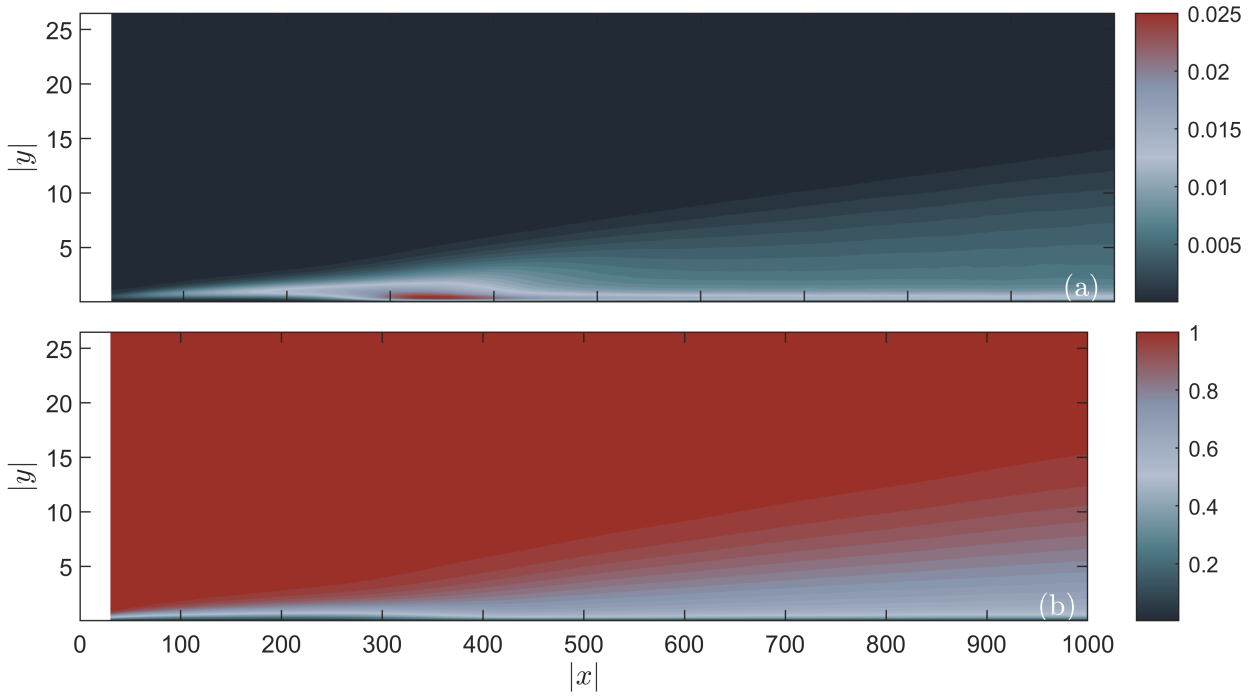

Figure 4.1: (a) the time and spanwise averaged streamwise velocity, u, of the flow. (b) The perturbation energy of the streamwise velocity u.

4.1 Turbulence Boundary Layer Data

The Boundary Layer (BL) data is sourced from Johns Hopkins Turbulence Data Base (JHTDB) [20, 14, 43]. The flow depicted in the dataset undergoes a bypass transition, with the transitional phase occurring at approximately $x \approx 350L_p$. Here, x represents the dimensional distance from the leading edge, and L_p denotes the half-thickness of the plate. This transition location is evident in the plot of skin friction coefficient, C_f, against the momentum Reynolds number, Re_Θ, as illustrated in Figure 4.2.

It should be noted that all length scales in this dataset are nondimensionalized by L_p. As a result, in this dataset, the Reynolds number based on the half-plate thickness, $Re_{L_p} = \frac{U_\infty L_p}{\nu} = 800$. The time-averaged streamwise velocity is depicted in Figure 4.1. What's more the minimum y location in the wall unit is $y^+_{min} = (u_\tau y)/\nu = 0.124$. This is later used to define convection velocities.

We confined our analysis to the laminar region of the flow, consistent with the assumption of linearity. This range can be estimated by looking at its skin-friction coefficient given by Ref. [43], as shown in Figure 4.2. The results shown in the result section are all to the left

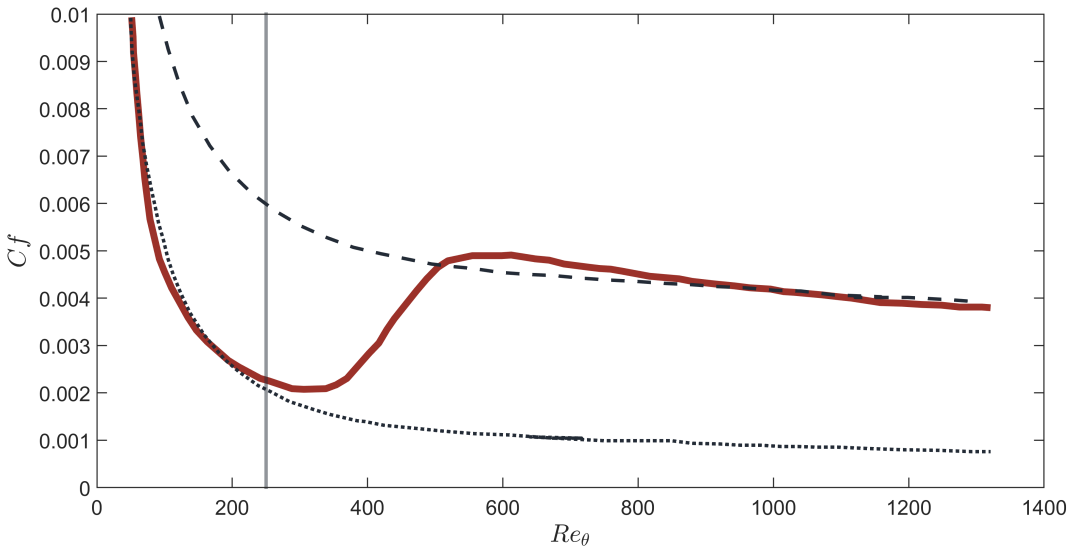

Figure 4.2: Skin-friction coefficient of the data (—) compare to laminar (····) and turbulent (- - -) estimations.

of this vertical line.

4.2 Data Matrix Construction for Boundary Layer Data

Under the assumption of linearity, we can analyze flow in the frequency domain, given that there are no cross-spectral interactions. This means that a Discrete Fourier Transform (DFT) can be conducted both in the spanwise direction and over time. This approach offers two advantages. Firstly, it reduces computation time, as analyzing the data at a specific wavenumber β and frequency ω reduces the original 4D matrix to 2D. Additionally, it enables the examination of flow properties at various frequencies and facilitates comparisons with results from other modal analyses.

The data matrix is structured so that m similar blocks of data are present at each streamwise location, capturing the spatial-temporal evolution of flow structures. The proposed procedure is illustrated in Figure 4.3. Figure 4.3 (a) shows the raw data as a four-dimensional matrix of size $[N_x, N_y, N_z, N_t] = [556, 112, 1024, 4701]$. In Figure 4.3 (b), an DFT is performed in the spanwise direction, and a single wavenumber, β, is selected, reducing the data

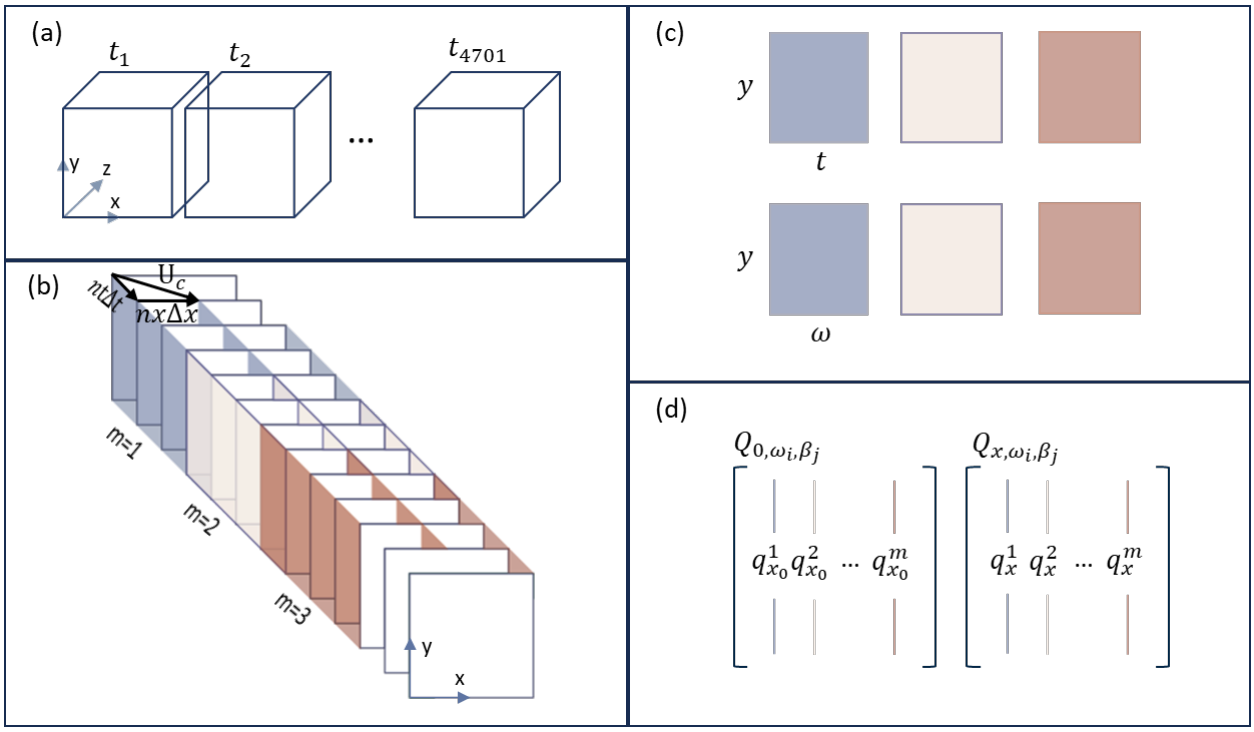

Figure 4.3: The procedures to obtain input to our algorithm.

dimension to three. Realizations are chosen at each x location, with a certain level of overlap demonstrated. Three realizations are shown for illustration purposes. As time progresses, the blocks of realizations also advance in time. The ratio of spatial to temporal steps is dictated by the concept of convection velocity, U_c, aiming to capture identical flow structures in each block and thus keep the spatial-temporal development within each realization's span. In Figure 4.3 (c), each realization has a size of $[N_y, N_{t_{block}}]$. An additional DFT is applied in the time direction for each realization at every x location, with $N_{t_{block}}$ defining the frequency range under consideration. Performing steps (b) and (c) for all three velocity components and selecting one ω results in Figure 4.3 (d), where the transformed data is organized into matrices $Q_{x,\omega_i,\beta_j} \in [n, m]$, with $n = 3N_y$. This methodology effectively captures the spatial-temporal development of the flow with a minimal input matrix size.

The colored blocks selected in steps (b) and (c) are defined by two parameters: the size of the block, `tsize`, and the step length in time, `tstep`. `tsize` dictates the range of frequencies we aim to investigate. Together, these two parameters determine the number of realizations that can be obtained from the limited 4701 time steps. Besides, under the linear assumption, Equation (4.2) is exact only in an infinity frequency domain. However, this requires taking Fourier transform to an infinite time block, which is unrealistic. In practice, we must take finitely long transforms. Under this constraint, we maximize the causal relationship between

Q_0 and Q_t by taking these transforms on temporal windows that are staggered in time.

To advance these blocks in the streamwise direction, they are also shifted in time. A previously mentioned convection velocity, U_c, is chosen to quantify these shifts. This value helps us follow the evolution of a specific fluctuation. According to Refs. [5, 38], U_c is defined as

$$U_c = \arg\max_U \int_{-\infty}^{+\infty} R(Ut, t)dt, \tag{4.3}$$

where $R(r_x, r_t)$ represents a spatial-temporal two-point correlation. An exact U_c can be calculated from Equation (4.3). However, our method does not rely on the precise value of U_c. A robust method should be independent of specific parameters. In this case, we aim for the convection velocity to fall within a range that keeps the flow structures within the selected state matrices. Therefore, we may choose a value around a typical nondimensionalized $U_c^+ = U_c/U_\tau \approx 10$ as provided by Refs. [5, 38], where U_c is nondimensionalized by the friction velocity U_τ. A simple derivation below converts this quantity to the shifting parameters, $\mathtt{n_x}$ and $\mathtt{n_t}$, as defined in Figure 4.3 (b). Note that in the domain of interest, the data is equally spaced in x with a constant time step, allowing the distance skipped in x and t to be expressed as $\mathtt{n_x}\Delta x$ and $\mathtt{n_t}\Delta t$. In the dataset, $\Delta x/L_p = 0.5844$ and $\Delta t = 0.25L_p/U_\infty$. The dimensional U_c in Figure 4.3 can then be expressed as

$$U_c = \frac{\mathtt{nx}\Delta x}{\mathtt{nt}\Delta t} \tag{4.4}$$

$$= \frac{\mathtt{nx}}{\mathtt{nt}}\left(\frac{\Delta x}{L_p}L_p\frac{U_\infty}{0.25L_p}\right) \tag{4.5}$$

$$= \frac{\mathtt{nx}}{\mathtt{nt}}\left(\frac{\Delta x}{L_p}\frac{U_\infty}{0.25}\right). \tag{4.6}$$

Nondimensionalizing U_c by U_∞ yields

$$\frac{U_c}{U_\infty} = 4\frac{\mathtt{nx}}{\mathtt{nt}}\frac{\Delta x}{L_p}. \tag{4.7}$$

As previously given in Chapter 1,

$$y_{min}^+ = \frac{u_\tau y_{min}}{\nu} = 0.124 \tag{4.8}$$

$$\frac{y_{min}}{L_p} = 0.0036 \tag{4.9}$$

Table 4.1: Example `nx` and `nt` with corresponding U_c^+.

`nx`	`nt`	U_c^+
1	3	18.12
1	4	13.59
1	5	10.87
1	6	9.06

By substituting Equation (4.9) into Equation (4.8), and with $Re_{L_p} = 800$, we have

$$\begin{aligned} \frac{U_\tau L_p}{\nu} &= \frac{0.124}{0.0036} \\ \frac{U_\tau}{U_\infty}\frac{U_\infty L_p}{\nu} &= \frac{0.124}{0.0036} \\ \frac{U_\tau}{U_\infty} &= \frac{0.124}{(0.0036)\,(800)} \\ &= 0.043. \end{aligned} \tag{4.10}$$

Combining Equation (4.7) and Equation (4.10), it is straightforward to derive that

$$\frac{U_c}{U_\tau} = 54.36\frac{\texttt{nx}}{\texttt{nt}} \tag{4.11}$$

Given that `nx` and `nt` are integers, the combinations close to $U_c/U_\tau \approx 10$ are listed in Table 4.1.

Through these steps, the input for our algorithm is clearly defined. In the following section, we present our results and compare them to previous findings obtained under parallel flow assumptions using operator-based methods.

4.3 Nondimensionalization of the Results

Before the discussion of the results, some adjustments to the coordinates and nondimensionalization need to be defined. Firstly, the x coordinates are updated to fit the Blasius boundary layer estimation. Since data from the simulation is stored starting from $x/L_p \approx 30$, along with the thickness of the leading edge, the result is not exactly Blasius. To compare with the operator solutions, a small manual adjustment of the streamwise location should be performed. As shown in Figure 4.4, The blue curve is the displacement thickness in the original x coordinate, and the dashed line is the displacement thickness of a Blasius boundary layer. It is obvious that they have similar trends but start at different locations. As we

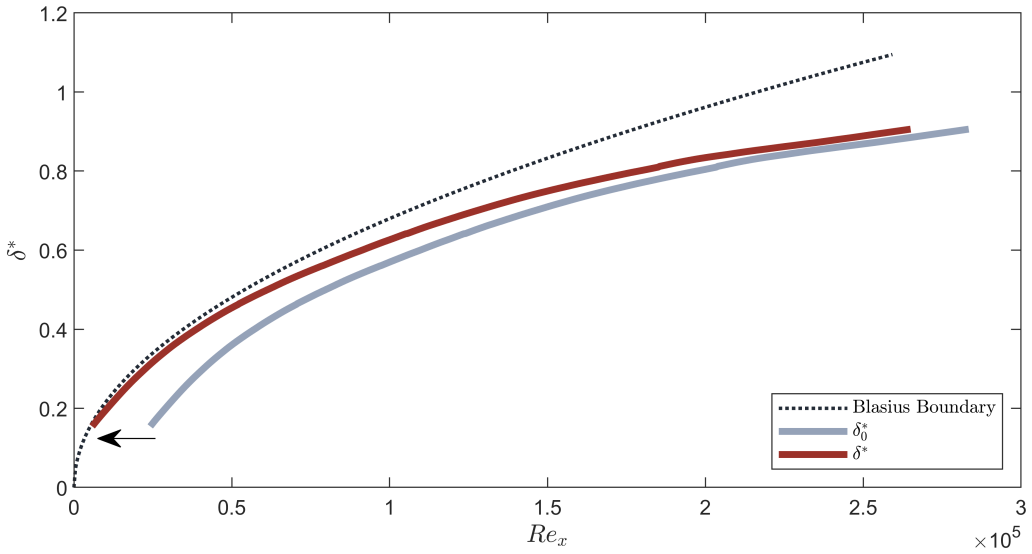

Figure 4.4: Adjusting the x coordinates to fit the Blasius boundary layer estimation.

moved the blue curve to its left as represented by the arrow, the new boundary layer, δ^*, is first aligned with the Blasius estimation and then diverges.

The new x coordinate is passed to define the nondimensionalization. Since the length scale in the simulation is the half-thickness of the plate, which does not have any physical meaning for boundary layer discussions, some other length scale should be used. In the streamwise location,

$$Re_x = \frac{U_\infty x}{\nu} = \frac{U_\infty L_p}{\nu}\frac{x}{L_p} = Re_{L_p}\frac{x}{L_p}. \tag{4.12}$$

Re_{L_p} is given in the dataset documentation while the x coordinate reported in the data is x/L_p. Meanwhile, the length scale of the wall-normal and spanwise directions are different according to Ref. [1, 15]. They scale these two directions with the boundary layer thickness. $\delta = \sqrt{\nu x/U_\infty}$ is defined, in the Blasius case $\delta = 1.72\delta^*$. The spanwise wavenumber, originally computed from the dataset should be βL_p. However, a proper nondimensionalization now should be $\beta\delta$. With previous defined Re_x and δ, $\beta\delta$ can be calculated as

$$\beta\delta = (\beta L_p)\left(Re_{L_p}\right)^{-1/2}\sqrt{\frac{x}{L_p}}. \tag{4.13}$$

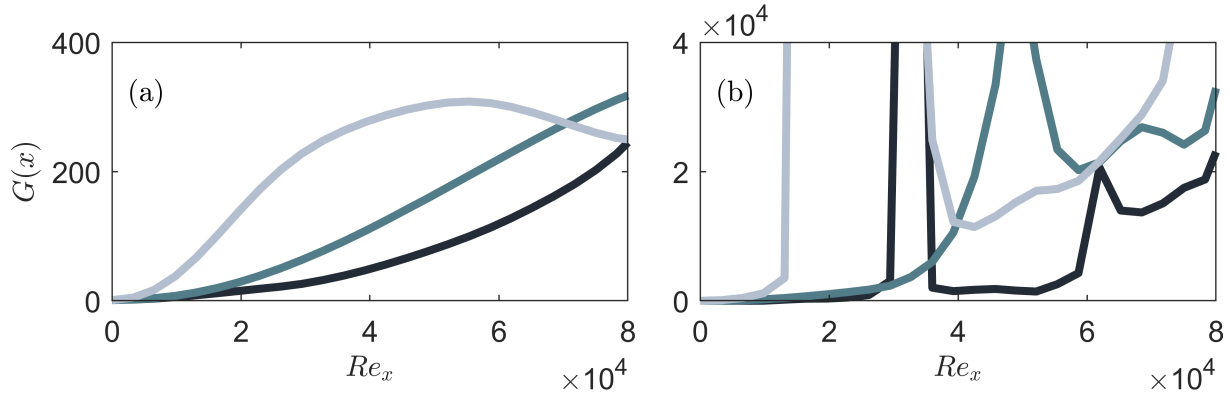

Figure 4.5: The growth over distance to the initial location in the data. ■, ■, ■represents $\beta\delta_{x_0} = [0, 0.1243, 0.2834]$. (a) is the result from IRM, while TLSM is shown in (b).

4.4 Result

Similar to the cases presented in Refs. [1, 15], we have examined scenarios for various β values and $\omega = 0$. Besides, according to the range of γ discussed in Chapter 3, we choose $\gamma = 0.01\lambda_{max}(\mathbf{Q}_0^*\mathbf{Q}_0)$.

The growth trends of the two regularization methods are depicted in Figure 4.5. In (a), we observe smooth growth, which we believe represents the transient growth in the flow, despite the curve not showing further decay in x for some wavenumbers. This could be attributed to the involvement of nonlinear terms. Even though we have simulated the nonlinearities with process noise, the nonlinear terms in this boundary layer data could have a larger magnitude and have correlations that further deviate the system from the linear assumption. Besides, the magnitude of the growth by IRM is sensitive to γ, unlike the GL case. However, the TLSM yields an incorrect result. The cause of this is not entirely clear; one potential explanation could be the insufficient number of realizations, m. Since TLSM involves initial projection into a low-dimensional POD space, this step could significantly reduce the accuracy of the result. Besides, TLSM is originally targeted to resolve measurement noise. It could be fundamentally different from this Direct Numerical Simulation (DNS) dataset, which has close to zero measurement noises and, potentially, a higher level of non-linearity. Both methods demonstrated good agreement with the literature results on the output mode of the streamwise velocity, u. As observed, except for the plots with high β values, parts (b), (c), (e), and (f) in Figure 4.6 show very close agreement with the findings in Refs. [1, 15], regardless of x or β. However, at zero β, a two-peak structure is observed. This structure bears resemblance to the Tollmien-Schlichting (T-S) modes as

described in Ref. [30]. Though it is aligned with the modal growth, which is strongest at $\beta = 0$, we cannot definitively claim these are the T-S modes. Further investigation is required to establish any connection with modal growth.

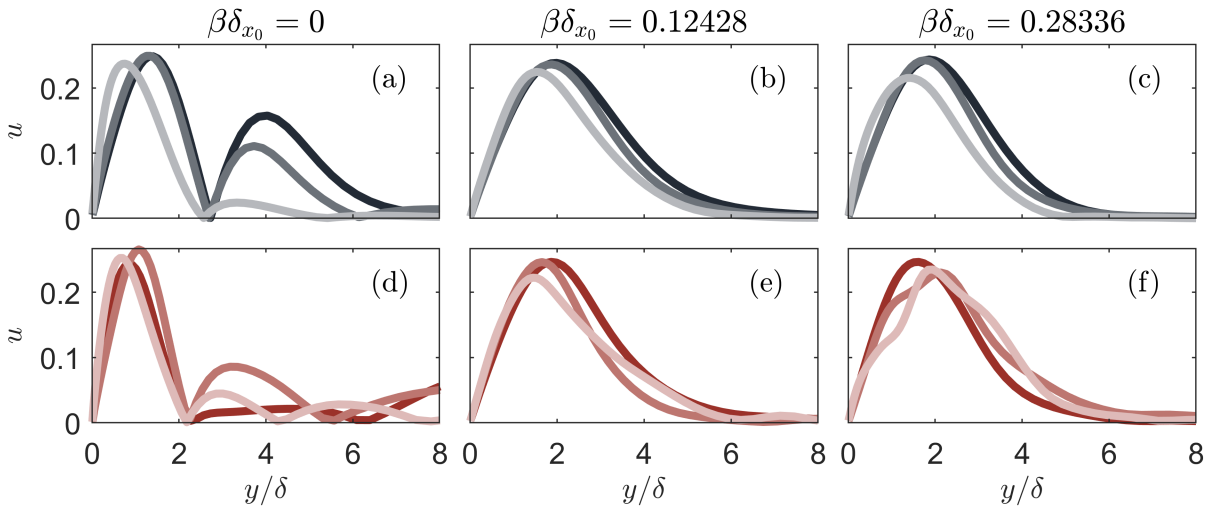

Figure 4.6: The output mode at $Re_x = [5.79, 8.41, 14.30] \times 10^4$ and $\beta\delta_{x_0} = [0, 0.124, 0.283]$. The top row shows results from IRM, and the bottom is from TLSM. Lighter colors represent higher in Re_x.

Finally, in Figure 4.7, we plotted the growth G/Re_x over $\beta\delta$, consistent to Refs. [1, 15]. Since according to them, G/Re_x approaches to a constant when $\lim_{Re_x \to \infty}$. It shows that there exists a consistent frequency $\beta\delta \approx 0.52$, where the growth appears to peak. This shape and magnitude of the growth are also consistent with findings in Refs. [1, 15]. The curves converge at high Reynolds numbers, aligning with the literature. However, in their studies, the peak is expected to occur at $\beta\delta = 0.45$. Factors such as early bypass transition, lift-up mechanisms, or strong freestream perturbations might be influencing our results. Nonetheless, further investigation may necessitate more testing and simulations under different conditions. Overall, our results qualitatively match the theories for spatial transient growth.

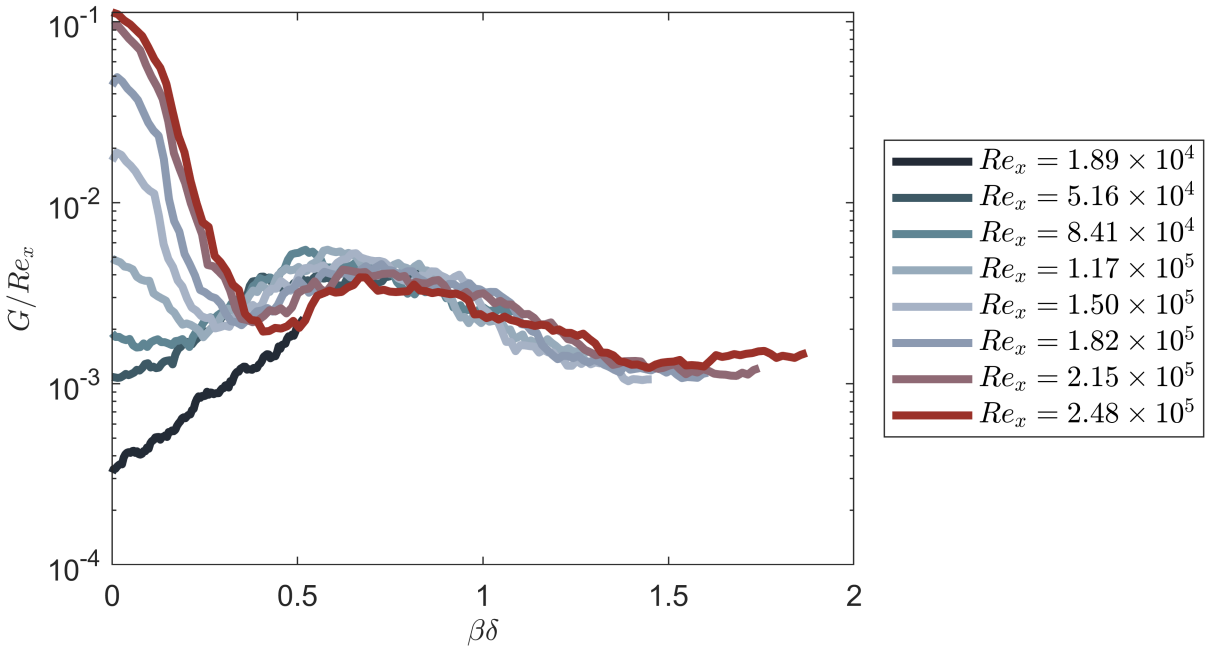

Figure 4.7: Growth over the spanwise frequency at different Re_x. The curves are smooth with `movmean` in MATLAB.

CHAPTER 5

Conclusion

This chapter summarizes the thesis and recommends some avenues for future work.

5.1 Summary of Contribution

In conclusion, we have developed a robust data-driven transient growth analysis method, which has been verified by comparing it with the operator-based solution of the GL equation. This method manifests its value by producing reasonable results in a non-parallel transitional boundary layer flow condition.

The data-driven method we proposed is derived from two distinct approaches. The LSAM modified the DMD, estimates the matrix exponential through the least squares method, and then calculates the SVD mode of it. This method is intuitive, as it directly involves taking a pseudoinverse of the resulting state. However, it is not immediately clear how this method relates to the maximization of energy. Consequently, the CFM was developed, starting from the principle of maximization. To solve the maximization problem, a Rayleigh quotient can be used.

For both methods, we developed regularization techniques to mitigate sensitivity to noise. The TLSM was selected as it is a well-justified method intended to enhance DMD. The IRM emerged naturally from CFM, effectively narrowing the gap between the maximum and minimum eigenvalues to prevent the inverse of the minimum eigenvalue from dominating the result. We compared these methods using the GL equation. From this comparison, TLSM's effectiveness was found to depend on the number of realizations, m largely. In contrast, IRM demonstrated robust consistency across different m and γ values. Although it introduces an additional parameter, we discussed a principled approach to selecting these parameters, highlighting the flexibility in their choice.

Lastly, we applied our method to the transitional boundary layer to identify spatial transient growth. It is noted that our method is limited when facing the nonlinearities in the flow

data. This can be easily noticed when the growth curve becomes jagged. Thus it is important to select data that might majorly contain linear growth of perturbations. Our prediction for the output mode of the streamwise velocity component aligns closely with operator-based results. We also identified a spanwise frequency that contributes significantly to transient energy growth. The discrepancies between our results and the literature include differences in the growth over the streamwise location and the spanwise frequency that maximizes energy growth. Investigating these differences would be the focus of future studies.

5.2 Future Work

This method still holds significant potential for further investigation. The future of this approach can be broadly categorized into two directions: completing the analysis of spatial transient growth and extending its application to other fields. The expected trajectory for each direction is discussed below.

As highlighted in Chapter 4, there remain some unanswered questions in the results. For instance, why does the growth not decay before increasing further for a range of spanwise wavenumber? Can this method also capture modal growth? What constitutes the optimal mode for the spanwise and wall-normal velocities? Several aspects can be explored to address these questions. Firstly, nonlinearity may undermine our method, prompting us to identify when nonlinearity begins to dominate the flow and its impact. One approach could involve adjusting the strength of inflow perturbations to observe their effects on the transition location and the corresponding changes in our method's results. Moreover, for the TLSM, the step involving modal reduction could be updated to employ methods other than POD, potentially offering a more robust capture of spatial-temporal flow information. A comprehensive understanding of our method's performance in spatial growth would enrich our knowledge of both the methodology and the physics of the transitional boundary layer.

Given that our method is data-driven, it is inherently adaptable to various flow conditions. A particularly promising area is hypersonic flow transitions. As noted by Ref. [27], flow transition in these high-speed environments is intricately linked to skin friction, thermal performance, and the acoustics of high-speed vehicles, where linear stability analysis tools also play a crucial role. This underscores the potential motivation and capability of our method to contribute to the analysis of hypersonic flows.

BIBLIOGRAPHY

[1] Paul Andersson, Martin Berggren, and Dan S Henningson. Optimal disturbances and bypass transition in boundary layers. *Physics of Fluids*, 11(1):134–150, 1999.

[2] Shervin Bagheri, Dan S Henningson, J Hoepffner, and Peter J Schmid. Input-output analysis and control design applied to a linear model of spatially developing flows. 2009.

[3] Hugh Maurice Blackburn, Dwight Barkley, and Spencer J Sherwin. Convective instability and transient growth in flow over a backward-facing step. *Journal of Fluid Mechanics*, 603:271–304, 2008.

[4] CD Cantwell, Dwight Barkley, and HM Blackburn. Transient growth analysis of flow through a sudden expansion in a circular pipe. *Physics of Fluids*, 22(3), 2010.

[5] Haecheon Choi and Parviz Moin. On the space-time characteristics of wall-pressure fluctuations. *Physics of Fluids A: Fluid Dynamics*, 2(8):1450–1460, 1990.

[6] Scott TM Dawson, Maziar S Hemati, Matthew O Williams, and Clarence W Rowley. Characterizing and correcting for the effect of sensor noise in the dynamic mode decomposition. *Experiments in Fluids*, 57:1–19, 2016.

[7] A Dotto, D Barsi, D Lengani, and D Simoni. A data-driven optimal disturbance procedure for free-stream turbulence induced transition. *Physics of Fluids*, 34(12), 2022.

[8] AA Draad and FTM Nieuwstadt. The earth's rotation and laminar pipe flow. *Journal of Fluid Mechanics*, 361:297–308, 1998.

[9] Peter Frame and Aaron Towne. Beyond optimal disturbances: a statistical framework for transient growth. *Journal of Fluid Mechanics*, 983:A2, 2024.

[10] L Hårkan Gustavsson. Energy growth of three-dimensional disturbances in plane poiseuille flow. *Journal of Fluid Mechanics*, 224:241–260, 1991.

[11] Maziar S Hemati, Clarence W Rowley, Eric A Deem, and Louis N Cattafesta. Debiasing the dynamic mode decomposition for applied koopman spectral analysis of noisy datasets. *Theoretical and Computational Fluid Dynamics*, 31:349–368, 2017.

[12] Dan S Henningson, Anders Lundbladh, and Arne V Johansson. A mechanism for bypass transition from localized disturbances in wall-bounded shear flows. *Journal of Fluid Mechanics*, 250:169–207, 1993.

[13] Lennart S Hultgren and L Håkan Gustavsson. Algebraic growth of disturbances in a laminar boundary layer. *The Physics of Fluids*, 24(6):1000–1004, 1981.

[14] Yi Li, Eric Perlman, Minping Wan, Yunke Yang, Charles Meneveau, Randal Burns, Shiyi Chen, Alexander Szalay, and Gregory Eyink. A public turbulence database cluster and applications to study lagrangian evolution of velocity increments in turbulence. *Journal of Turbulence*, (9):N31, 2008.

[15] Paolo Luchini. Reynolds-number-independent instability of the boundary layer over a flat surface: optimal perturbations. *Journal of Fluid Mechanics*, 404:289–309, 2000.

[16] John L Lumley. *Stochastic tools in turbulence*. Courier Corporation, 2007.

[17] John Leask Lumley. The structure of inhomogeneous turbulent flows. *Atmospheric turbulence and radio wave propagation*, pages 166–178, 1967.

[18] Vasudevan Mukund and Björn Hof. The critical point of the transition to turbulence in pipe flow. *Journal of Fluid Mechanics*, 839:76–94, 2018.

[19] William M'F Orr. The stability or instability of the steady motions of a perfect liquid and of a viscous liquid. part ii: A viscous liquid. In *Proceedings of the Royal Irish Academy. Section A: Mathematical and Physical Sciences*, volume 27, pages 69–138. JSTOR, 1907.

[20] Eric Perlman, Randal Burns, Yi Li, and Charles Meneveau. Data exploration of turbulence simulations using a database cluster. In *Proceedings of the 2007 ACM/IEEE Conference on Supercomputing*, pages 1–11, 2007.

[21] W Pfenniger and GV Lachman. Boundary layer and flow control. *GV Lachmann, ed*, 2:970, 1961.

[22] Satish C Reddy and Dan S Henningson. Energy growth in viscous channel flows. *Journal of Fluid Mechanics*, 252:209–238, 1993.

[23] Eli Reshotko. Transient growth: A factor in bypass transition. *Physics of Fluids*, 13(5):1067–1075, 2001.

[24] Osborne Reynolds. Xxix. an experimental investigation of the circumstances which determine whether the motion of water shall be direct or sinuous, and of the law of resistance in parallel channels. *Philosophical Transactions of the Royal society of London*, (174):935–982, 1883.

[25] Clarence W Rowley. Model reduction for fluids, using balanced proper orthogonal decomposition. *International Journal of Bifurcation and Chaos*, 15(03):997–1013, 2005.

[26] Clarence W. Rowley and Scott T.M. Dawson. Model reduction for flow analysis and control. *Annual Review of Fluid Mechanics*, 49(1):387–417, 2017.

[27] William S Saric, Eli Reshotko, and Daniel Arnal. Hypersonic laminar-turbulent transition. *AGARD ADVISORY REPORT AGARD AR*, 2:2–2, 1998.

[28] Herman Schlichting. Berechnung der anfachung kleiner störungen bei der plattenströmung. *ZAMM*, 13(171-174):50, 1933.

[29] Peter J Schmid. Dynamic mode decomposition of numerical and experimental data. *Journal of fluid mechanics*, 656:5–28, 2010.

[30] Peter J Schmid, Dan S Henningson, and DF Jankowski. Stability and transition in shear flows. applied mathematical sciences, vol. 142. *Appl. Mech. Rev.*, 55(3):B57–B59, 2002.

[31] Jeffrey P Slotnick, Abdollah Khodadoust, Juan Alonso, David Darmofal, William Gropp, Elizabeth Lurie, and Dimitri J Mavriplis. Cfd vision 2030 study: a path to revolutionary computational aerosciences. Technical report, 2014.

[32] Arnold Sommerfeld. *Ein beitrag zur hydrodynamischen erklaerung der turbulenten fluessigkeitsbewegungen*. 1909.

[33] Kunihiko Taira, Steven L Brunton, Scott TM Dawson, Clarence W Rowley, Tim Colonius, Beverley J McKeon, Oliver T Schmidt, Stanislav Gordeyev, Vassilios Theofilis, and Lawrence S Ukeiley. Modal analysis of fluid flows: An overview. *Aiaa Journal*, 55(12):4013–4041, 2017.

[34] Vassilios Theofilis. Advances in global linear instability analysis of nonparallel and three-dimensional flows. *Progress in aerospace sciences*, 39(4):249–315, 2003.

[35] Nils Tillmark and P. Henrik Alfredsson. Experiments on transition in plane couette flow. *Journal of Fluid Mechanics*, 235:89–102, 1992.

[36] Walter Tollmien. Über die entstehung der turbulenz. *Vorträge aus dem Gebiete der Aerodynamik und verwandter Gebiete: Aachen 1929*, pages 18–21, 1930.

[37] A. Towne, O. T. Schmidt, and T. Colonius. Spectral proper orthogonal decomposition and its relationship to dynamic mode decomposition and resolvent analysis. *J. Fluid Mech.*, 847:821–867, 2018.

[38] Aaron Towne, Adrián Lozano-Durán, and Xiang Yang. Resolvent-based estimation of space–time flow statistics. *Journal of Fluid Mechanics*, 883:A17, 2020.

[39] Aaron S Towne. *Advancements in jet turbulence and noise modeling: accurate one-way solutions and empirical evaluation of the nonlinear forcing of wavepackets*. PhD thesis, California Institute of Technology, 2016.

[40] Jonathan H. Tu, Clarence W. Rowley, Dirk M. Luchtenburg, Steven L. Brunton, and J. Nathan Kutz. On dynamic mode decomposition: Theory and applications. *Journal of Computational Dynamics*, 1(2):391–421, 2014.

[41] I Wygnanski, Mo Sokolov, and D Friedman. On transition in a pipe. part 2. the equilibrium puff. *Journal of Fluid Mechanics*, 69(2):283–304, 1975.

[42] Israel J Wygnanski and FH Champagne. On transition in a pipe. part 1. the origin of puffs and slugs and the flow in a turbulent slug. *Journal of Fluid Mechanics*, 59(2):281–335, 1973.

[43] Tamer A Zaki. From streaks to spots and on to turbulence: exploring the dynamics of boundary layer transition. *Flow, turbulence and combustion*, 91:451–473, 2013.